Journal Pre-proof

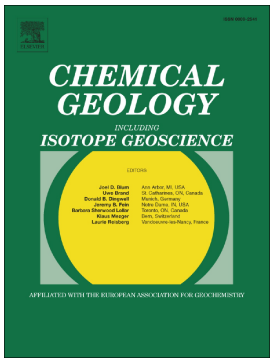

Protocols for in situ measurement of oxygen isotopes in goethite by ion microprobe

H.S. Monteiro, P.M. Vasconcelos, K.A. Farley, J.N. Ávila, H.B.D. Miller, P. Holden, T.R. Ireland

PII: S0009-2541(19)30565-0

DOI: https://doi.org/10.1016/j.chemgeo.2019.119436

Reference: CHEMGE 119436

To appear in: *Chemical Geology*

Received date: 16 December 2018

Revised date: 27 November 2019

Accepted date: 28 November 2019

Please cite this article as: H.S. Monteiro, P.M. Vasconcelos, K.A. Farley, et al., Protocols for in situ measurement of oxygen isotopes in goethite by ion microprobe, *Chemical Geology* (2019), https://doi.org/10.1016/j.chemgeo.2019.119436

Protocols for *in situ* measurement of oxygen isotopes in goethite by ion microprobe

Monteiro, H.S.[1*], Vasconcelos, P.M.[2,4], Farley, K.A.[4], Ávila, J.N.[3], Miller, H.B.D.[4], Holden, P.[3], and Ireland, T.R.[3]

[1]*Departamento de Planejamento Territorial e Geoprocessamento, Universidade Estadual Paulista, Rio Claro 13506-900, Brazil*

[2]*School of Earth and Environmental Sciences, The University of Queensland, Brisbane, Queensland 4072, Australia*

[3]*Research School of Earth Sciences, The Australian National University, Canberra, ACT 2601, Australia*

[4]*Division of Geological and Planetary Sciences, California Institute of Technology, Pasadena, CA 91125, USA*

** Corresponding author:*

H.S. Monteiro

Universidade Estadual Paulista

Departamento de Planejamento Territorial e Geoprocessamento

Rio Claro, SP 13.506-900

Phone: (55) (19) 3526-9347 (Office)

Keywords: goethite, SHRIMP-SI, (U-Th)/He, oxygen isotopes, ion microprobe, matrix effect

ABSTRACT

We present protocols for high-spatial resolution measurement of oxygen isotope ratios of goethite (α-FeOOH) with the Sensitive High Mass Resolution Ion Microprobe – Stable Isotopes (SHRIMP-SI) and propose a natural sample as a potential goethite reference material (RM) for ion microprobe analysis. We assess the effects of goethite chemical composition, crystallographic orientation, and texture on the accuracy and repeatability of SHRIMP-SI $\delta^{18}O$ ($\delta^{18}O_{SIMS}$) results. Synthetic goethites evaluated as potential $\delta^{18}O_{SIMS}$ RM are powdery, porous, and finely crystalline; they do not yield repeatable results. A dense colloform goethite from the Capão topaz mine, Minas Gerais, Brazil, fulfills major prerequisites: it is stoichiometrically relatively pure, yields repeatable oxygen isotope results, and occurs in abundance to produce a RM for long-term use. We use an average laser fluorination $\delta^{18}O_{LF\text{-}VSMOW}$ value of -17.3 ± 0.3 ‰ (1SD) obtained for five aliquots of this RM to normalize all $\delta^{18}O_{SIMS}$ measurements. Multiple $\delta^{18}O_{SIMS}$ analyses of a large fragment of the Capão L4 (CL4) RM analyzed in three different runs yield an overall repeatability of -17.3 ± 0.5 ‰ (2SD, n = 294) for all three runs combined. Natural variability and crystal orientation effects are the main reasons for the excess spread of the $\delta^{18}O_{SIMS}$ results compared to the spot internal precision (ca. 0.2 ‰). All $\delta^{18}O_{SIMS}$ analyses (n=1027) in various aliquots of CL4, randomly oriented and analyzed in 26 sessions during eight distinct runs, yield an overall repeatability of ± 0.7 ‰ (2SD), confirming that CL4 is a suitable SIMS RM. After ascertaining its suitability as a RM, we used CL4 to standardize analyses of other natural goethite samples with the SHRIMP-SI and compared $\delta^{18}O_{SIMS}$ and laser fluorination results to test the relationship between natural properties (e.g., porosity, minor elements substituting for Fe), preparation procedures (e.g., polish and relief), instrument conditions, and the overall precision and accuracy of the SIMS analyses. Samples containing minor elements substituting for Fe (e.g., Al, Mn, Cu, Zn, etc.) or as contaminants (e.g., Si, P) require significant matrix corrections. Because we could not find homogenous natural goethite samples showing a large range in metal concentrations, we extrapolate our calibration curves beyond the composition of our calibration goethite samples. $\delta^{18}O_{SIMS}$ results corrected for instrument mass fractionation (using CL4) and compositionally dependent matrix effects (using several calibration goethites of known elemental composition) are less precise but statistically indistinguishable from their laser fluorination results. However, porous samples are unsuitable for SHRIMP-SI $\delta^{18}O$ analysis. Dense colloform samples yield repeatable results for individual growth bands, showing that the high spatial resolution, moderate precision, and speed of analysis of the SHRIMP-SI can resolve variations in oxygen isotope composition acquired during sample growth. (U-Th)/He geochronology of equivalent aliquots from the same goethite samples reveal that the combination of the two methods permits

the extraction of temporal variation in the isotopic compositions of meteoric solutions in the geological past.

1. INTRODUCTION

The oxygen isotope composition of goethite (α-FeOOH) is a useful environmental indicator applied in the reconstruction of the isotopic signature of ancient waters and past surface temperatures on Earth (Yapp, 1987, 1993,1997, 2000, 2001, 2008; Bird et al., 1992, 1993; Girard et al., 1997, 2000, 2002; Poage et al., 2000; Sjostrom et al., 2004; Yapp and Shuster, 2011; Miller et al., 2017). The basic assumption of goethite as an environmental indicator is that it precipitates in isotopic equilibrium with water, and that the goethite-water $^{18}O/^{16}O$ fractionation factor $\alpha_{(gth\text{-}water)}$ – determined from mineral precipitation experiments, calculated theoretically, or derived from mineral-water exchange reactions – is well known. Fractionation factors depend primarily on temperature, but they may also depend on pH, solution composition, and rate of precipitation (Yapp, 1990, 2007, 2012; Müller, 1995; Bao and Koch, 1999; Zheng, 1998). Natural goethites show $\delta^{18}O$ values ranging from ~ -16 to +4 ‰ (Yapp, 2001), reflecting the wide range in the isotopic composition of meteoric precipitation due to latitude- and elevation-driven Rayleigh fractionation. The stable isotope composition of goethite may be determined using fluorination and carbon reduction bulk methods, which require ~ 20 mg of material (Yapp, 1987). Laser fluorination techniques offer the advantage of requiring < 2 mg of pure sample (Girard et al., 1997; Miller et al., 2017). Both approaches have been successfully used in measuring the oxygen isotope composition of natural goethite from diverse settings to characterize paleoenvironments (e.g., Bird et al., 1992; Poage et al., 2000; Bao et al., 2000; Miller et al., 2017).

Despite these successes, a major challenge in determining the isotopic composition of goethite is the fact that it commonly forms colloform aggregates of fine crystals oriented parallel to the direction of mineral precipitation, where each growth band may be smaller than 50 μm (Figure 1a). The refinement and application of (U-Th)/He dating to natural goethite show that sequential bands in colloform goethite may span millions of years (Shuster et al., 2005; Heim et al., 2006; Vasconcelos et al., 2013). Variations in minor and trace element compositions from one band to another suggest that parental solutions change in elemental – and probably also isotopic – composition through time. In addition, goethite masses often show evidence for partial dissolution before resumption of colloform growth (Figure 1b), contain cross-cutting veins of late-stage goethite generations (Figure 1b), and may be intimately intergrown with hypogene or supergene minerals (e.g., quartz, kaolinite, gibbsite, cryptomelane, cuprite, malachite, etc.; Figure 1b) of potentially different isotopic compositions. Bulk analysis of these samples produces a composite

$\delta^{18}O$ value for the distinct generations of goethite plus the mineral contaminants possibly present within the goethite masses, and chemical analysis and material balance calculations must be applied to derive the $\delta^{18}O$ value of the end-member goethite (Yapp, 1987). Therefore, determining the $\delta^{18}O$ value of a single generation of goethite may require µm-scale resolution. Importantly, in situ analysis with µm-scale resolution also improves our confidence in bulk analysis. For example, in many situations, laser fluorination analysis on ~ 2 mg samples, averaging a few hundreds to a few thousand years of mineral precipitation, may still resolve important environmental and paleoclimatic questions (e.g., Miller et al., 2017), particularly where high resolution in situ analyses shows that average results are representative of individual mineral precipitation events.

We explore the refinement of suitable approaches to use the sensitive high-resolution ion microprobe – stable isotopes (SHRIMP-SI) (Ireland, 2004; Ireland et al., 2008) to measure the $\delta^{18}O$ value of goethite at scales (µm) necessary to resolve single mineral precipitation events. We also combine SHRIMP-SI $^{18}O/^{16}O$ measurements with laser-heating (U-Th)/He dating of the same goethite sample to refine the spatial resolution of time-calibrated goethite $\delta^{18}O$ studies (e.g., Miller et al., 2017). The spatial resolution of the (U-Th)/He method (~ 200 µm), when combined with that of SHRIMP-SI $^{18}O/^{16}O$ analysis (~25 µm), offers the opportunity to study, at previously unattainable scales, environmental conditions during mineral precipitation at specific times in the geological past. Obtaining accurate SHRIMP-SI $^{18}O/^{16}O$ measurements, however, requires a well-characterized reference material (RM). In addition, sample- and instrument-related bias, such as the potential dependence of ionization efficiency and instrumental mass fractionation (IMF) on chemical composition, crystallographic orientation, sample porosity, texture, and relief (e.g., Eiler et al., 1997; Vielzeuf et. al., 2005; Kita et al., 2009, 2010; Ickert and Stern, 2013), must be addressed.

In this study, we characterize, test, and propose a suitable goethite reference material (RM). We estimate the precision potentially attainable with SHRIMP-SI $\delta^{18}O_{SIMS}$ by analyzing several hundred spots on a large fragment of the RM in three separate SHRIMP-SI runs. Once convinced that our RM is suitable, we use it to correct for instrument mass fractionation (IMF) during each run. We test the accuracy of SHRIMP-SI $\delta^{18}O_{SIMS}$ results obtained using our RM by comparing laser fluorination $\delta^{18}O_{LF\text{-}VSMOW}$ and SHRIMP-SI $\delta^{18}O_{SIMS}$ measurements for a sample that has the same composition and crystallographic properties of our proposed RM. We further test the accuracy of SHRIMP-SI $\delta^{18}O_{SIMS}$ results by comparing SIMS and laser fluorination values for a suite of mineralogically pure and homogenous calibration goethites that differ in minor and trace element contents from the RM (EA1). Discrepancies between SIMS and LF results show that IMF

is partially dependent on goethite chemical composition (matrix effect). We implement two distinct matrix corrections: one based on the total Fe contents of our RM and calibration goethites; and one based on the total content of elements other than Fe in the RM and calibration goethites. We assess the validity of the matrix corrections by comparing $\delta^{18}O_{LF\text{-}VSMOW}$ and matrix corrected SHRIMP-SI $\delta^{18}O_{SIMS}$ for each of the calibration samples. Once ascertaining that appropriate IMF and matrix corrections permit obtaining reliable $\delta^{18}O$ values for our calibration goethites, we use our validated RM to investigate potential crystallographic effects on measured $\delta^{18}O$ values. We also assess other sample-related parameters (e.g., porosity) that may affect isotopic analysis with the SHRIMP-SI and offer guidelines on sample selection criteria and preparation to maximize the chance of successful $\delta^{18}O_{SIMS}$ analyses.

Finally, we selected a sample of Fe-duricrust blanketing the Gandarela Plateau, Quadrilátero Ferrífero, Brazil (Monteiro et al., 2014, 2018), to demonstrate the potential of the $\delta^{18}O_{SIMS}$ method to extract information recorded on complex assemblages of goethites, representing many generations and recording superimposed weathering events spanning ~ 40 Ma. Importantly, the prolonged weathering and paleoclimatic histories for the site in southeastern Brazil are based on the textural, elemental, geochronological, and $\delta^{18}O_{SIMS}$ analyses of a single 3x3x3 cm goethite sample, attesting to the power of high spatial resolution analysis of supergene phases.

2. SUITABLE SHRIMP-SI $^{18}O/^{16}O$ GOETHITE REFERENCE MATERIAL (RM)

Goethite is the orthorhombic iron oxyhydroxide α-FeOOH, a phase that is isostructural with diaspore (AlOOH), groutite (MnOOH), and bracellewite (CrOOH) (Cornell and Schwertmann, 1996). Structural similarities allow solid solution of Al, Mn, and Cr, but also Ni, Co, V, Cu, Zn, Pb, and a variety of other minor and trace (e.g., U and Th) elements, into natural goethites (Cornell and Schwertmann, 1996). Consequently, pure Fe-end member goethite is rare. Coarse-grained, well-crystallized stoichiometric goethites commonly show ~ 10% structural water. For these goethites, expected non-stoichiometric OH^- is minimum. In addition, goethite forms by a variety of processes, such as in situ incongruent oxidative dissolution of Fe^{2+}-bearing phases, Fe^{3+}-metasomatism of porous rocks and minerals at the Earth's surface, oxidation and direct precipitation of Fe^{2+} from slightly acidic and reducing solutions, direct precipitation of Fe^{3+} from acid solutions, etc. Variable compositions and complex textures, possibly including intergrown mineral phases, pose some challenges in selecting and validating a suitable goethite RM for ion microprobe analysis. A suitable RM must be chemically and isotopically homogenous and exist in large enough quantity to yield material that, once characterized and validated, can be made available to the wider scientific community for independent comparisons.

To ensure mineralogical purity, we focused our search for a RM on goethites precipitated directly from solution into empty cavities. These samples form colloform masses that are generally devoid of mineral contaminants. From a suite of several hundred goethite samples collected over two decades from various weathering profiles in Brazil, Australia, New Caledonia, Africa, China, and the USA, we selected a large and massive goethite cobble collected in a colluvium in the vicinity of the Capão topaz mine, Minas Gerais, Brazil. The sample is composed of cm-wide growth bands (Figure 2) for which we had previous information on age and trace element homogeneity. The massive colloform goethite cobble from the Capão mine was sliced, polished, and growth bands displaying distinct visual characteristics were arbitrarily defined as Layers 1 to 5 (CL1 to CL5) (Figure 2). Layers CL1, CL2, CL4, and CL5 were microdrilled and analyzed as described below. We also precipitated and tested synthetic goethite as potential RMs, as synthetic goethite has been successfully used to investigate goethite–water $^{18}O/^{16}O$ fractionation (Yapp, 2007).

3. ANALYTICAL TECHNIQUES

Goethite slices and micro-cores (~1-2 cm long and 5 mm internal diameter (ID)) were retrieved from the hand specimens (e.g., Figure 2; EA 1), crushed to 0.1 – 2 mm grains, ultrasonicated in tap water (~ 20 min), distilled water (~ 10 min), rinsed in ethanol, and air-dried. Clean goethite grains were mounted in 2.54 cm OD acrylic disks specially designed for the SHRIMP-SI during this study, filled with epoxy, polished, imaged by optical and electron microscopy, and investigated by SEM/EPMA before or after ion microprobe analysis. In addition to goethite grains, cm-size fragments from the Capão goethite sample (Figure 2) were also mounted in epoxy and polished for analysis (EA2). Selected areas or grains were targeted for optical and scanning electron microscopy (SEM), electron microprobe analysis (EPMA), X-ray diffraction (XRD), (U-Th)/He geochronology, laser fluorination (LF), and SHRIMP-SI oxygen isotope analysis. Images for all polished disks containing RM, calibration samples, and unknown goethite grains are shown in EA 2.

3.1. Optical and Scanning Electron Microscopy

Polished blocks and thin-sections were investigated by transmitted- and reflected-light optical microscopy and by SEM/BSE (secondary electron and back-scattered electron images) to determine goethite textures, mineral assemblages, paragenetic relationships, modes of precipitation, and sample purity.

3.2. Electron Microprobe Analysis

Electron microprobe analyses were performed with a JEOL JXA-8200 at the Centre for Microscopy and Microanalysis (CMM) of the University of Queensland, Brisbane, Australia. Standards and unknowns were carbon coated under the same conditions. Analyses were performed using a beam current of 15 nA, accelerating voltage of 15 kV, and focused spot size of one μm (except for more volatile elements, for which spot size was increased to 10 μm). Between 14 and 21 elements were measured in each individual analytical session using the standards and calculated detection limits listed in EA3.

3.3. X-ray Diffraction

Goethite samples were analyzed by bench-top powder XRD, following analytical and data reduction procedures outlined in Monteiro (2017), to ascertain that they were indeed pure and well crystallized. Some of the samples (Roy Hill and Winsor) were also analyzed by synchrotron X-ray diffractometry at the Australian National Beamline Facility (ANBF) or the Photon Factory, National Laboratory for High Energy Physics (KEK), Tsukuba, Japan, as outlined in Heim (2006), Waltenberg (2012), and Vasconcelos et al. (2013).

3.4. Synthetic Goethite

Goethite powders were precipitated at various temperatures (22, 30, and 40°C) and two different pHs (<2 and >12) (Mostert, 2014). For the high pH experiments, solutions were prepared by adding 125 ml of 1 M $Fe(NO_3)_3.9H_2O$ to 125 ml of 5 M KOH into high density polyethylene (HDP) bottles. For the low pH experiments, 350 ml of 1 M $Fe(NO_3)_3.9H_2O$ plus 175 ml 2 M HNO_3 were diluted with 175 ml H_2O. 140 ml of this bulk solution was than mixed with140 ml of 1 M NaOH in a HDP bottle. The solutions were stored in 500 ml bottles for a minimum period of 74 days to permit adequate crystal growth. Goethite precipitates were split into three or more 50 ml centrifuge tubes, topped up with distilled water, and centrifuged for 28 min. The supernatant was then decanted, the tube filled with distilled water a second time, and sonicated for 15 min. The tube containing the goethite residue and distilled water was once again centrifuged for the same period. This procedure was repeated at least three times to ensure that all unwanted salts were removed. All precipitates were dried in air and stored in closed tubes (Mostert, 2014). Mineralogical composition and crystallographic properties of synthetic goethite aliquots were determined by Synchrotron Powder Diffraction at the Australian Synchrotron (Mostert, 2014).

3.5. (U-Th)/He analysis

Goethite samples were analyzed by (U-Th)/He geochronology at Caltech following the procedures outlined in Monteiro et al. (2014). For He extraction, individual goethite aliquots were

encapsulated in Pt tubes, loaded into wells in a copper disk, placed in a sample chamber, and heated (900 °C) with a diode laser under vacuum for 6 minutes. To ensure total He extraction, Pt capsules were heated a second time, also for 6 minutes, at the same temperature. After He extraction was completed, degassed samples were transferred to Teflon containers where they were dissolved in concentrated ultrapure HCl (closed vials were placed in the oven at 90°C for 12h), spiked with known amounts of ^{235}U and ^{230}Th, evaporated and re-dissolved in concentrated ultrapure HNO_3, diluted in Milli-Q water and analyzed by ICP-MS.

3.6. Laser fluorination analysis

Goethite samples were analyzed by laser fluorination at Caltech following procedures outlined in Miller et al. (2017). The reported $\delta^{18}O_{LF\text{-}VSMOW}$ values are single or multiple measurements carried out on 1-3 mg of sample (Table 3). Several aliquots of the UWG-2 garnet standard measured throughout the runs yield average $\delta^{18}O_{LF\text{-}VSMOW}$ values of 5.4 ± 0.1 ‰ (1σ, n=4), 5.5 ± 0.01 ‰ (1σ n=2), 5.5 ± 0.5 ‰ (1σ, n=4), 5.4 ± 0.3 ‰ (1σ, n=7), and 5.4 ± 0.1 ‰ (1σ, n=4). $\delta^{18}O_{LF\text{-}VSMOW}$ values of unknowns were corrected for the difference between measured and accepted values of the UWG-2 garnet standard ($\delta^{18}O_{VSMOW}$ = 5.8‰) (Valley et al., 1995).

Our RM and calibration goethites were also analyzed at the University of Oregon stable isotope laboratory following procedures outlined by Bindeman et al. (2008). Multiple aliquots of the UOG garnet standard analyzed together with the unknowns yield average $\delta^{18}O_{VSMOW}$ values of 6.3 ± 0.3 ‰ (1σ), 6.5 ± 0.01 ‰ (1σ), and 6.6 ± 0.2 ‰ (1σ). $\delta^{18}O$ values of unknowns were corrected for the difference between measured and accepted values of the UOG garnet standard ($\delta^{18}O$ = 6.5 ‰) (Valley et al., 1995).

3.7. In situ analysis of oxygen isotopes by SHRIMP-SI

Goethite aliquots from individual samples, subsampled from the same batch of washed grains used for (U-Th)/He geochronology, were placed in individual pits in a 37-pit disk mount (EA2). We also mounted large goethite chips and grains on glass slides covered with doubled-face tape (EA2; e.g., HM-23) to facilitate mounting oriented grains. Loaded mounts were filled with epoxy under vacuum to minimize air bubbles. Sample mounts were lapped, polished to 0.25 μm, and imaged with a Leica DM6000M automated microscope. All mounts were cleaned with detergent and ethanol, dried in vacuum at 60 °C, coated with gold, and kept under vacuum at 60 °C for at least two days before analysis. A total of 13 disks were mounted with grains of CL4, goethite calibration samples (for which we had laser fluorination results), and unknowns (EA2; four unknowns are presented and discussed in this article). All disks contained at least 2 grains of CL4

in different geometric positions. One disk hosted two 1.5 cm-long fragments of the Capão colloform goethite sample (containing CL1, CL2, CL3, and CL4 bands; EA2) to test the isotopic homogeneity of the RM (CL4) and goethite calibration samples (e.g., CL1 and CL2).

Oxygen isotope measurements were carried out during eight analytical runs, from October 2014 to September 2017, using the SHRIMP-SI at ANU (Ávila et al, in press; Ireland et al., 2008, 2014). Each run lasted from one to five days, and a single run includes several analytical sessions, defined by the disk analyzed during a segment of the run. The instrument was tuned at the beginning of each session, and tuning parameters may have varied slightly from session to session. Rarely, within a session (e.g., RUN7-session HM23), the instrument may have had to be retuned if significant drift was detected; after retuning, a new session was started (e.g., RUN7-session HM23B).

Goethite grains were sputtered with a Cs^+ primary beam with initial acceleration potential of +5 kV from the ion gun. At the sample surface, the acceleration potential was held at ~ -10 kV, producing a final collision energy of 15 keV at the target (Ireland et al., 2014). An elliptical beam spot of ~ 20 x 25 μm was used for all sessions. The low and high mass head detectors equipped with Faraday cups were used for simultaneous detection of $^{16}O^-$ and $^{18}O^-$. The electrometers measuring $^{16}O^-$ and $^{18}O^-$ were set to 10^{11} Ω (50V range) and 10^{11} Ω (5V range), respectively. The collector slit widths were set at 400 μm for $^{16}O^-$ and 300 μm for $^{18}O^-$, and potential isobaric interferences on $^{18}O^-$ from $^{17}OH^-$ and $^{16}OD^-$ were well resolved. Oxygen measurements consisted of five or six acquisition cycles of 20s, each cycle comprising ten 2 s integrations for a total acquisition time of about 2 min. The $^{18}O/^{16}O$ ratio is the weighted average of five or six cycles.

Initially, we collected $\delta^{18}O_{SIMS}$ analyses of several goethite samples to test their repeatability. After a trial run suggested that our choice of potential RM – CL4 – was indeed homogeneous and yielded repeatable results, we focused on quantifying its isotopic homogeneity and suitability as a RM (based on the measurement repeatability), and the ultimate precision to be expected from SIMS analysis of this goethite. We analyzed, in three separate sessions, 294 points on a single 1.5 cm block of the Capão goethite containing a large band of CL4 (Figure 2, EA 2). We further tested the precision possible with SIMS analysis of goethite by interpreting the entire population of CL4 SHRIMP-SI analyses for all eight runs (n=1027), as discussed below.

After ascertaining that CL4 was indeed a suitable RM and that it yielded moderately reproducible results (± 0.5-0.7 ‰ [2 SD], when compared to ± 0.2-0.4 ‰ [2 SD] routinely attained for garnets), we used it to analyze several natural goethite samples, varying in compositions and modes of precipitation, for calibration purposes (samples illustrated and briefly described in EA1).

Calibration goethites and unknowns were analyzed in sequences of 10-12 spots interspersed with blocks of 3-4 spots on CL4 RM. The instrumental mass fractionation ($\alpha_{IMF\text{-}CL4}$) for a session is calculated following equation 1 below:

$$\alpha_{IMF\text{-}CL4} = \frac{R_{CL4}^{raw}}{\left(R_{VSMOW} \cdot \left(1+\delta^{18}O_{LF}/1000\right)\right)} \quad (1)$$

where R_{CL4}^{raw} is the raw mean $^{18}O/^{16}O$ value for a group of CL4 analyses; R_{VSMOW} is the $^{18}O/^{16}O$ of the Standard Mean Ocean Water (0.0020052; Baertschi, 1976); and $\delta^{18}O_{LF}$ is the known laser fluorination value of the CL4 RM. In this study, values of $\alpha_{IMF\text{-}CL4}$ varied between 0.979 and 0.991 across 26 sessions. If drift occurred during a session, all analyses were drift corrected. Drift corrections, applied via the analysis of CL4 throughout each session, were sufficient to compensate for the effects of instrument-related variations, such as sputtering, ionization, transmission, and detection. This correction is directly applied during data reduction using the ANU software POXI.

Raw values measured on calibration and unknown goethites were corrected for instrument mass fractionation according to the equations below:

$$R_{cal}^{CL4} = R_{cal}^{raw} / \alpha_{IMF\text{-}CL4} \quad (2)$$

$$R_{unk}^{CL4} = R_{unk}^{raw} / \alpha_{IMF\text{-}CL4} \quad (3)$$

where $\alpha_{IMF\text{-}CL4}$ is defined as above; R_{cal}^{raw} and R_{unk}^{raw} are the raw $^{18}O/^{16}O$ values for calibration and unknown goethites, respectively; and R_{cal}^{CL4} and R_{unk}^{CL4} are $^{18}O/^{16}O$ for calibration and unknown goethites, respectively, corrected for IMF, as determined from the analysis of the CL4. This correction is also directly applied during data reduction using the ANU software POXI. An initial $\delta^{18}O^*_{SIMS}$ value is then calculated using equation 4 below:

$$\delta^{18}O^*_{SIMS\text{-}cal} = \left(\left(\frac{R_{cal}^{CL4}}{R_{VSMOW}}\right) - 1\right) \times 1000 \quad or \quad \delta^{18}O^*_{SIMS\text{-}unk} = \left(\left(\frac{R_{unk}^{CL4}}{R_{VSMOW}}\right) - 1\right) \times 1000 \quad (4)$$

The IMF-corrected values for calibration goethites and unknowns, as derived above, should be close to their true value (as measured by laser fluorination) if the calibration and unknown

goethites have compositions similar to that of the reference material CL4. If goethite compositions differ from that of CL4, an additional matrix correction is necessary:

$$\alpha_{matrix\text{-}cal} = \frac{R_{cal}^{CL4}}{R_{cal}^{t}} \quad (5)$$

$$\alpha_{matrix\text{-}unk} = \frac{R_{unk}^{CL4}}{R_{cal}^{t}} \quad (6)$$

Substituting 2 in 5 and rearranging:

$$R_{cal}^{t} = \frac{R_{cal}^{raw}}{\alpha_{\text{IMF-CL4}} \times \alpha_{matrix\text{-}cal}} \quad (7)$$

Similarly, substituting 3 in 6 and rearranging:

$$R_{unk}^{t} = \frac{R_{unk}^{raw}}{\alpha_{\text{IMF-CL4}} \times \alpha_{matrix\text{-}unk}} \quad (8)$$

Where R_{cal}^{t} and R_{unk}^{t} R_{unk}^{t} are the true values (as measured by laser fluorination) of the calibration samples and unknowns, respectively, and $\alpha_{\text{IMF-CL4}}$ and α_{matrix} are as defined in equations (1), (5) and (6) above.

We apply matrix correction following the procedures outlined in Martin et al. (2014). After correcting the raw values for IMF ($\alpha_{\text{IMF-CL4}}$), as outlined above, we define the remaining difference between the $\delta^{18}O^{*}_{SIMS}$ value for the calibration or unknown goethites and its laser fluorination $\delta^{18}O_{LF}$ value as the $Bias_{matrix}$:

$$Bias_{matrix} = \delta^{18}O^{*}_{SIMS} - \delta^{18}O_{LF} \quad (9)$$

To correct for compositionally dependent matrix effects, we used the total Fe or the sum of the average concentrations of all minor elements [V+Co+P+Cr+Al+Ni+Mn+Si+Pb+Cu+Ti+Zn] in the calibration goethites, as measured by EMPA. For every run, we calculate an average $Bias_{matrix}$ value for each calibration goethite. We plot the average $Bias_{matrix}$ values for our RM and each calibration goethite against their chemical compositions in two different ways, as described below, from which we generate equations to be applied for correction of all calibration goethites and unknowns analyzed in that run.

3.7.1 $Bias_{matrix}$ correction based on Fe content

Pure stoichiometric goethite should contain 62.86 wt% Fe. Elements substituting for Fe will lower its content proportionally, which could affect sputtering characteristics and ionization efficiency (Fe-dependent matrix effect). To correct measured $\delta^{18}O^*_{SIMS}$ values for Fe-dependent matrix effects, we use the total average Fe contents measured by EMPA to plot the values of $Bias_{matrix}$ against Fe content for each calibration goethite analyzed in all the runs (EMPA listed in Table 1 and illustrated in EA4). Linear regressions through the correlation plots generated for all the runs together are used to produce an equation that relates Fe-contents to $Bias_{matrix}$ ($Bias_{Fe}$):

$$Bias_{Fe} = -0.74\ (\pm\ 0.13)\ x + 45.71\ (\pm\ 7.72)\ [r^2 = 0.49] \quad (8)$$

where x is the average Fe content (wt%) of the calibration goethite, as illustrated in Figure 3a and summarized in Table 1.

We used the value of $Bias_{Fe}$ to calculate the "true" $\delta^{18}O_{\text{"true"}}$ value for each calibration goethite:

$$\delta^{18}O_{Fe\text{-"true"}} = \delta^{18}O^*_{SIMS} - Bias_{Fe} \quad (9)$$

Comparisons of $\delta^{18}O_{Fe\text{-"true"}}$ with $\delta^{18}O_{LF}$ for each calibration and unknown goethites measured in our experiments show that one single equation to calculate $Bias_{Fe}$, lumping together all runs, does not properly reconcile SIMS and LF results. Therefore, we apply the same approach outlined above and generate a compositionally dependent regression to calculate $Bias_{Fe}$ for each run separately, as illustrated in Figure 3c. This run-specific approach provides the most accurate results ($\delta^{18}O_{Fe\text{-"true"}}$) as deduced by the match between $Bias_{Fe}$-corrected $\delta^{18}O_{SIMS}$ and $\delta^{18}O_{LF}$ values. Even more accurate reconciliation between $\delta^{18}O_{SIMS}$ and $\delta^{18}O_{LF}$ values would be possible if we were to carry out linear regressions for each session separately. Whether a more accurate and precise reconciliation is worth the additional analytical time required to achieve it will depend entirely on the nature of the scientific question to be answered.

3.7.2 $Bias_{matrix}$ correction based on content of all elements replacing iron

Goethite may accommodate Al, Mn, Cr, Ni, Co, Cu, Ti, Pb, and Zn substituting for Fe. Substitution of these elements may also affect ion probe sputtering characteristics and ionization efficiency, resulting in compositionally dependent matrix effects. But in addition to elements in solid solution, natural goethites often show elevated Si and P contents (Table 1, EA4,5). It is unlikely that these elements replace Fe^{3+} in octahedral coordination in the α-FeOOH structure, but their presence, irrespective of crystallographic site, will result in lowered Fe contents as

determined by EPMA, and should also affect ion probe sputtering characteristics and ionization efficiency. Therefore, we use the sum of the average concentrations of [V+Co+P+Cr+Al+Ni+Mn+Si+Pb+Cu+Ti+Zn] measured by EMPA in our calibration goethites to generate a linear regression for all runs lumped together; the linear regression is used to apply a correction for $Bias_{ALL}$, as outlined below:

$$Bias_{ALL} = 1.93\ (\pm\ 0.46)\ x - 2.65\ (\pm\ 0.97)\ [r^2 = 0.33] \quad (10)$$

where x is the sum of the average [V+Co+P+Cr+Al+Ni+Mn+Si+Pb+Cu+Ti+Zn] content (wt%) of each calibration goethite (Figure 3b, Table 1).

Similarly to the matrix corrections based on total Fe contents, a universal regression for all runs does not produce the most accurate matrix-corrected $\delta^{18}O_{SIMS}$ values, as determined by the accuracy of the equality below:

$$\delta^{18}O^*_{SIMS} - Bias_{ALL} = \delta^{18}O_{LF} \quad (11)$$

Therefore, we use linear regressions generated for each separate run to implement matrix corrections based on the [V+Co+P+Cr+Al+Ni+Mn+Si+Pb+Cu+Ti+Zn] contents of our calibration goethites, and to calculate the $\delta^{18}O_{ALL\text{-}true}$ for each calibration goethite, as summarized in Figure 3d.

3.7.3 Error analysis

The final error reported for each $\delta^{18}O_{SIMS}$ result must include the following uncertainties (Ickert and Stern, 2013): (1) within spot uncertainty or internal error; (2) repeatability uncertainty; (3) instrument mass fractionation uncertainty; (4) reference material LF uncertainty; (5) matrix effect uncertainty; and (6) elemental analysis uncertainty used for calibrating matrix effects.

Within spot uncertainty (e) is associated with internal errors related to signal and detector noise, and it is defined as (Martin et al., 2014):

$$e = \sqrt{\frac{1}{\sum_i^n \frac{1}{e_i^2}}} \quad (12)$$

where n is the number of scans of ^{18}O and ^{16}O measurements on each spot (n = 5 or 6, in our case), and e_i is the standard deviation of 10 sub-count $^{18}O/^{16}O$ ratios. This uncertainty is automatically calculated by POXI, and it is reported for individual SHRIMP-SI spot results throughout the analytical session. Typical values ranged from 0.1 to 0.2 ‰.

The repeatability uncertainty depends on instrument factors, grain homogeneity and orientation, and the number of spot analyses. It is the standard error (95% CI) of a population of spot analysis on the CL4 RM (e_{CL4}) analyzed under the same conditions as the unknowns throughout a run. Repeatability uncertainty for each group of CL4 RM analysis, for each population of CL4 analyzed within a session throughout the eight runs, are summarized in Table 4. Values range from ± 0.06 to ± 0.33 ‰ (1 SE).

The IMF uncertainty $\left(s_{R_{CL4}^{RAW}}\right)$ is the instrument mass fractionation uncertainty determined relative to CL4 propagated into individual spot analysis (Ickert and Stern, 2013). It is determined by the confidence limits in the mean R_{CL4}^{raw} $\left(s_{R_{CL4}^{RAW}}\right)$ for an analytical session, as reported in Table 4. The IMF uncertainty is computed into the within spot uncertainty (e) above throughout the run.

The reference material (CL4) uncertainty $\left(s_{R_{CL4}^{t}}\right)$ reflects how well we know the value of the RM with respect to its true value, as determined by laser fluorination. We adopted the $\delta^{18}O_{LF}$ value of -17.3 ± 0.3 ‰ for CL4 for the reasons discussed in the results and discussion sections below.

Matrix effect uncertainties $\left(s_{a_{matrix}}\right)$ are calculated as the residuals (σ_{Fe} and σ_{ALL}) on the linear regressions of Bias versus Fe or [V+Co+P+Cr+Al+Ni+Mn+Si+Pb+Cu+Ti+Zn] contents measured for the RM and calibration goethites for each run separately (equations 13 e 14). This is the major uncertainty factor in all our SIMS measurements.

$$\sigma_{Fe} = \sqrt{\frac{1}{N}\sum_{i=1}^{N}\left(Bias - \widehat{bias}\right)^2} \quad (13)$$

$$\sigma_{ALL} = \sqrt{\frac{1}{N}\sum_{i=1}^{N}\left(Bias - \widehat{bias}\right)^2} \quad (14)$$

Where $\widehat{bias}$ is the predicted bias by the linear correlation and N is the number of RM and calibration goethites used in the regression (Martin et al., 2014).

Finally, uncertainties in quantifying the Fe and Fe-substituting element (V, Co, P, Cr, Al, Ni, Mn, Si, Pb, Cu, Ti and Zn) contents of calibration materials and unknown goethite samples by electron microprobe analysis must be accounted for in the final $\delta^{18}O_{SIMS}$ uncertainty.

The final uncertainty for each analysis was calculated either as

$$s_{d^{18}O} \approx \sqrt{e^2 + e_{CL4}{}^2 + s_{R^t_{CL4}}{}^2 + s_{a_{Fe\text{-}matrix}}{}^2 + s_{Fe\text{-}EPMA}} \quad (15)$$

or

$$s_{d^{18}O} \approx \sqrt{e^2 + e_{CL4}{}^2 + s_{R^t_{CL4}}{}^2 + s_{a_{ALL\text{-}matrix}}{}^2 + s_{ALL\text{-}EPMA}} \quad (16)$$

The results and errors for each spot analysis, without compositionally controlled matrix corrections and with either $\left(s_{a_{Fe\text{-}matrix}}\right)$ or $\left(s_{a_{ALL\text{-}matrix}}\right)$ corrections, are plotted (Figures 6, 7) for each calibration goethite, as discussed below.

4. RESULTS

4.1. Electron microprobe results

Figure 2 illustrates the average elemental composition of CL1, CL4, and CL5 growth bands. Table 1 shows the average composition of RM and each calibration goethite investigated in this study; complete analytical results are available in EA5 and are plotted in EA4. The CL4 goethite shows nearly stoichiometric concentrations of Fe and O (Figure 2) and less than 2 wt% total minor and trace element contents. All samples selected as calibration goethites show relatively low but still significant minor and trace element contents (Table 1; EA4,5). No absolutely pure stoichiometric α-$FeOOH_{goe}$ was found among the many samples screened for this study (Table 1; EA4,5).

4.2. X-ray diffraction results

Figure 4 illustrates XRD patterns for CL4 and some of our calibration goethites. Rietveld refinement for a representative aliquot of CL4 indicates that goethite is the only identifiable mineral. Trace veins of Mn oxides, observed in reflected-light optical and scanning electron microscopy in CL4, are not detectable by XRD. All XRD patterns show crystalline goethites devoid of significant contaminant contents, except for small quartz peaks in all samples other than CL4 (Figure 4).

4.3. Synthetic Goethite SHRIMP-SI test

Given the rarity of natural stoichiometrically pure α-FeOOH, and aiming to avoid $\delta^{18}O_{SIMS}$ uncertainties associated with matrix-effects related to minor elements substituting for Fe, we investigated the potential suitability of synthetic goethite (Mostert, 2014) as SHRIMP-SI RM. Their purity, known temperature of precipitation, and the known composition of the water from which the α-FeOOH precipitated should make synthetic goethites ideal RMs for the SHRIMP-SI.

As discussed below, the finely crystalline texture of the synthetic material, its porous nature, and the heterogeneous pellets produced when the synthetic powders were agglomerated under a 10-30-ton/cm^2 hydraulic press show that synthetic goethite is not suitable as a SHRIMP-SI RM unless large homogeneous single crystals were to be experimentally grown.

4.4. (U-Th)/He ages

(U-Th)/He ages for replicate aliquots of CL4 and other calibration samples are summarized in Table 2. All samples yield reproducible or very narrow ranges of results for the replicates, suggesting that, at least within the spatial and chronological resolution of the (U-Th)/He method, they are homogeneous. (U-Th)/He ages among samples range from ~ 284 to ~ 3.5 Ma. Most of the goethites show low U (< 10 ppm) and Th (< 1 ppm) contents, except for sample Win 06 03A, which contains between 150 – 317 ppm U and 9 – 18 ppm Th, and sample BAHLGB, which contains between 81 – 76 ppm U. All goethite samples show low Th/U ratios.

4.5. Laser fluorination analysis

Table 3 lists laser fluorination $\delta^{18}O_{LF\text{-}VSMOW}$ values for CL4 and all calibration goethites. EA7 provide laser fluorination $\delta^{18}O_{LF\text{-}VSMOW}$ values for four additional unknown goethite samples. We use the average [-17.3 ± 0.3 ‰ (1SD)] of five $\delta^{18}O_{LF\text{-}VSMOW}$ [-17.22 ± 0.03, -17.72 ± 0.05, -17.27 ± 0.02,-16.90 ± 0.05, and -17.34 ± 0.02 ‰ (1SD)] analyses done at Caltech as the correct value of the primary CL4 RM for the reasons discussed below. Two aliquots of the CL4 RM analyzed in the University of Oregon laboratory yielded $\delta^{18}O_{LF\text{-}VSMOW}$ results of -16.34 and -16.33 ± 0.2 ‰. The reason for the discrepancy between the laser fluorination results from the two laboratories is not fully known. Natural heterogeneity in the stable isotope composition of samples may account for some of the variability, but the reproducibility among the five aliquots analyzed at Caltech and the two aliquots analyzed at Oregon suggests an analytical, as opposed to a sample heterogeneity, issue. Noticeably, samples CL1 and CL2 (from the same hand-sample from which CL4 was obtained) also show discordant results between the Caltech and Oregon laboratories (Oregon results are ~ 1 ‰ heavier than the Caltech results, Table 3). Unfortunately, the limited number of laser fluorination results available precludes ascertaining the real variability related to isotopic composition heterogeneity. Total oxygen yield varied between 84 and 115% (except for one analysis of sample Win01B for which oxygen yield was 37% – this result was ignored – and one analysis of sample CL1 for which oxygen yield was 54%).

4.6. SHRIMP-SI $^{18}O/^{16}O$ analysis

4.6.1. Reference material and calibration goethites

Using the $\delta^{18}O_{LF\text{-}VSMOW}$ value of -17.3 ± 0.3 ‰ (1σ) for our primary RM (CL4), we measured the raw $\delta^{18}O_{SIMS}$ values for a variety of samples ranging in mode of precipitation, composition, textures, and porosity (Table 4, EA1); the complete dataset is given in the supplementary resource EA6. Multiple analyses (n=294) for one large block of CL4 investigated in three distinct runs are illustrated in Figure 5a. A comprehensive set of results for several aliquots of CL4 analyzed in eight SHRIMP-SI runs are illustrated in Figure 5b. These results illustrate the repeatability that delimits the ultimate precision obtainable by SHRIMP-SI $\delta^{18}O_{SIMS}$ goethite investigations using CL4 as the RM in our runs.

IMF-corrected $\delta^{18}O_{SIMS}$ values, based on the analysis of CL4, are obtained for CL1, CL2, and CL5 and compared to their laser-fluorination $\delta^{18}O_{LF\text{-}VSMOW}$ results (Figure 6a-c). IMF- and matrix-corrected (based on Fe contents – $Bias_{Fe}$) $\delta^{18}O_{SIMS}$ values for two of the same samples (CL1 and CL5), together with their laser-fluorination $\delta^{18}O_{LF\text{-}VSMOW}$ values, are shown in Figure 6d,e. IMF- and matrix-corrected (based on [V+Co+P+Cr+Al+Ni+Mn+Si+Pb+Cu+Ti+Zn] contents – $Bias_{ALL}$) $\delta^{18}O_{SIMS}$ values for CL1 and CL5 and their laser-fluorination $\delta^{18}O_{LF\text{-}VSMOW}$ values are shown in Figure 6f, g. The significance of those results is discussed below.

Similar results for six calibration goethites of different compositions, corrected for IMF (Figure 7a-f), corrected for both IMF and matrix effects based on Fe contents (Figure 7 g-l), and corrected for IMF and matrix effects based on [V+Co+P+Cr+Al+Ni+Mn+Si+Pb+Cu+Ti+Zn] contents (Figure 7 m-r), all using the CL4 RM, are compared to their laser-fluorination $\delta^{18}O_{LF\text{-}VSMOW}$ values; the implication of the results are also discussed below.

4.6.2. Crystal orientation effect on $\delta^{18}O_{SIMS}$ results

To test whether goethite is subject to crystallographic effects (Lyon et al., 1998; Huberty et al., 2010; Kita et al., 2010) previously detected for other iron oxides, we mounted several goethite aliquots with the c-axis either parallel (Figure 8 a,b,e,f) or perpendicular (Figure 8c,g) to the plane of the sample mount. Fortunately, natural goethites grow preferentially along the c-axis, forming elongated needles, blades, or prismatic micro-crystallites with aspect ratios of 5-1000. These samples preferentially break into grains elongated along the c-axis (Figure 8); they will sit flat when placed on the sample mount, making mounting oriented grains viable.

SHRIMP-SI spot analysis for two aliquots of the Win-01B calibration goethite illustrated in Figure 8a-c are individually shown in Figure 8d. The results, -11.72 ± 0.07 ‰ (1 SE, n=6) for aliquots where the c-axis is parallel to the surface ablated by the Cs^+-beam (Figure 8a,b) and -12.23 ± 0.11 ‰ (1 SE, n=6) for aliquots where the c-axis is perpendicular to that plane (Figure

8c), show only a small difference in apparent $\delta^{18}O_{SIMS}$ with crystal orientation for this sample. In another example, two aliquots of the CL4 RM (Figure 8e-g) mounted with the c-axis parallel [$\delta^{18}O_{SIMS}$ values of -17.82 ± 0.11 ‰ (1 SE, n=4) and -17.05 ± 0.15 ‰ (1 SE, n=7)] and one aliquot mounted with c-axis perpendicular to the polished surface [$\delta^{18}O_{SIMS}$ value of -15.37 ± 0.11 ‰ (1 SE, n=4)] suggest a potential instrumental bias of 2.0 ± 0.2 ‰ (1 SE).

Another test for the susceptibility of SHRIMP-SI results to crystallographic orientation is provided in the experiment illustrated in Figure 9. In this experiment, a disk containing the CL4 RM and another disk containing additional grains of CL4 to be analyzed as unknowns were oriented as shown in Figure 9. The mount containing CL4 RM was kept in the same position throughout the experiment (Figure 9c). Three grains of CL4 goethite, with c-axes parallel to the surface (Figure 9a,d), were analyzed as unknowns, yielding the results plotted in Figure 9f. During the same run, the unknown disk was rotated 90° clockwise with respect to the Cs^+-beam, as illustrated in Figure 9b,e, and re-analyzed. The three aliquots yield average $\delta^{18}O_{SIMS}$ values of -17.0 ± 0.1 ‰ [G1] (1 SE), -17.1 ± 0.1 ‰ [G2] (1 SE), and -17.7 ± 0.1 ‰ [G3] (1 SE) before 90° rotation; and -19.2 ± 0.1 ‰ [G1_R] (1 SE), -18.3 ± 0.1 ‰ [G2_R] (1 SE), and -19.0 ± 0.1 ‰ [G3_R] (1 SE) after rotation. This test confirms that fractionation related to crystal orientation can potentially introduce an instrumental bias of ~ 1.7 ± 0.2 ‰ on $\delta^{18}O_{SIMS}$ values, considerably less than values observed for hematite (see discussion). The reasons for lower instrument crystal orientation bias on goethite, as compared to hematite, are not obvious.

4.6.3. Porosity effect on $\delta^{18}O_{SIMS}$ results

Porosity is another sample-related factor that may affect the SHRIMP-SI $^{18}O/^{16}O$ ratios. This feature was particularly noticeable in our attempts to analyze synthetic stoichiometric goethites (Figure 10). Successful analysis of synthetic samples would permit the development of stoichiometrically pure reference materials (and metal doped goethites to be used for matrix corrections). Unfortunately, synthetic samples were very fine-grained and porous. Attempts to eliminate pore spaces by agglomerating the finely crystalline goethite masses into pellets using a hydraulic press (~10-30 tons/cm^2) were unsuccessful. The pressed pellets still showed variable porosity after polishing (Figure 10), and the isotopic results from more porous areas differed from those of the less porous segments of the pellet (e.g., from - 3.82 ‰ to - 8.57 ‰ in a single sample), suggesting that it was not possible to eliminate the porosity problem. Various fragments of the pressed pellets also showed variations in isotopic composition and oxygen yields when analyzed by laser fluorination (H. Miller, unpublished results), suggesting that during sample

agglomeration under pressure goethite grains may acquire different water contents, ultimately affecting the isotopic signature of the sample fraction investigated.

Porosity also affects $\delta^{18}O_{SIMS}$ results in natural samples. For example, the grain illustrated in Figure 8a,b yields relatively reproducible results except for spots 6 and 7, which are discrepant by about +2‰ from the mean (Figure 8d). Petrographic observation shows that the two spots that yield discrepant results occur in a yellow porous zone in the grain (Figure 8b). Spot 5, sitting at the boundary between brown (nonporous) and yellow (porous) goethite, yields an intermediate value (Figure 8b,d).

4.6.4. Goethite texture effect on $\delta^{18}O_{SIMS}$ results

We also tested grain texture as a selection and vetting criterion when choosing samples to be analyzed and when interpreting results obtained from goethite analyses by the SHRIMP-SI. Figure 11 illustrates three goethite samples (BAH-F124-111.2B, BAH-F226-157.6, BAH-F124-123.2) displaying contrasting textures. We will show below the effect of these textures on SHRIMP-SI results.

Figure 11a illustrates a grain from sample BAH-F124-111.2B. $\delta^{18}O_{SIMS}$ values for spots for same-generation symmetrical bands from opposite sides of the cavity yield the results illustrated in Figure 11b. The entire dataset reveals a relatively homogeneous population with $\delta^{18}O_{SIMS}$ = 0.3 ± 0.1 ‰ (1 SE, n=56), which is the same as the $\delta^{18}O_{LF\text{-}VSMOW}$ result [0.4 ± 0.2 ‰ (1 SD)] obtained for an aliquot of this goethite (EA7). The apparent scatter in the $\delta^{18}O_{SIMS}$ results for bands I, III, and IV can be partially explained by the change in orientation of the goethite crystallites. For example, goethite crystallites sampled at spots 19 and 20 show an orthogonal orientation to crystallites analyzed at spots 11-16 in the same band (Figure 11a,b).

Two grains from the massive and homogeneous BAH-F226-157.6 goethite (Figure 11c,d) yield reproducible results within each grain, and the results illustrate the possible precision obtained when goethite textures are homogeneous. The increased precision permits resolving differences in $\delta^{18}O_{SIMS}$ values for the two grains from this sample. The average $\delta^{18}O_{SIMS}$ value for two grains [-2.5 ± 0.1 ‰ (SEM), n=21] is in good agreement with three out of four $\delta^{18}O$ laser fluorination results (-2.4 ± 0.01 ‰, -2.6 ± 0.01, -1.7 ± 0.02 ‰, and -2.5 ± 0.02 ‰; EA7).

In contrast, the porous, prismatic and randomly oriented goethite crystals in sample BAH-F124-123.2 (Figure 11e) yield more scattered data: -3.1 ± 0.4 ‰ (SEM, n=8) for Grain **1**; and -4.3 ± 0.4 ‰ (SEM, n=7) for Grain **2**; and, for the entire population, -3.7 ± 0.3 ‰ (SEM, n=15). Three

goethite grains from this sample yielded $\delta^{18}O_{LF\text{-}VMSOW}$ values of -2.7 ± 0.2 ‰ (1SD; Oregon), -1.4 ± 0.04 ‰, and -1.9 ± 0.03 ‰ (1SD; Caltech).

5. DISCUSSION

5.1. The CL4 SHRIMP-SI reference material

The Capão goethite is a large ~10 cm cobble collected from a colluvium near the Capão topaz mine: it is dense, massive, colloform, and well crystallized (Figure 2). Its colloform habit, wide growth bands, and chemical and mineralogical purity (as determined by electron microprobe analysis and X-ray diffractometry, respectively) (Figures 2,4; Table 1; EA2) suggest precipitation in an empty cavity. Acicular goethite crystals are closely packed and display c-axes oriented in the direction of sample growth (Figure 2), enabling mounting of oriented grains. To investigate its suitability as a SHRIMP-SI RM, we tested the repeatability of measurements obtained from a fragment of CL4 within a run and between three separate runs. Before discussing those results, we need to justify the $\delta^{18}O_{LF\text{-}VSMOW}$ adopted value of -17.3 ± 0.3 ‰.

There are seven laser fluorination $\delta^{18}O$ determinations for CL4 (Table 3). We were unable to obtain more laser fluorination results from a wider range of laboratories, despite repeated efforts. The limited number of measurements, coupled with the fact that the Caltech and Oregon results differ by nearly one ‰, demands either pooling the results into a single average number with a large uncertainty to be propagated to all SIMS results; or, alternatively, choosing among the results from the two laboratories. To decide on the most suitable approach, we used the average of the five Caltech values, the average of the two Oregon values, and the pooled seven results from the two laboratories to fit our SIMS results. For some of our calibration goethites, we calculated $\alpha_{IMF\text{-}CL4}$ using the three different numbers, and we compared the SIMS results, corrected for IMF ($\alpha_{IMF\text{-}CL4}$), and also corrected for composition variations ($\alpha_{Fe\text{-}matrix}$ by $Bias_{Fe}$ or $\alpha_{ALL\text{-}matrix}$ by $Bias_{ALL}$ corrections), with their laser fluorination values. The value of CL4 that resulted in the most consistent reconciliation between SIMS and LF results was the Caltech value of -17.3 ± 0.3 ‰, thus justifying its adoption in this study.

We analyzed 294 SHRIMP-SI 20 x 25 µm spots on a large fragment of the CL4 mounted as a single block. Instrumental drift was evaluated and corrected for, if necessary, as outlined in section 3.7 above. The $\delta^{18}O_{SIMS}$ values for each session in the three runs (Runs 7, 9, and 10) are reasonably precise (Table 4), suggesting that the proposed RM is isotopically homogeneous. All results for the eight sessions pooled together still yield a reasonably precise dataset (-17.3 ± 0.5 ‰, 2 SD, n=294) (Figure 5a), attesting to the compositional and isotopic homogeneity of CL4 and

confirming its suitability as a reference material for the SIMS. Lastly, results for all CL4 spot analysis from all 26 sessions in eight separate SHRIMP-SI runs, where crystal fragments may have been mounted in random orientations, still define a moderately precise dataset (-17.3 ± 0.7 ‰, 2 SD, n=1027) (Figure 5b), further substantiating CL4's suitability as a RM. Therefore, using CL4 as our RM, we tested the reliability of $\delta^{18}O_{SIMS}$ measurements by devising and applying two distinct types of matrix corrections and comparing $\delta^{18}O_{SIMS}$ with $\delta^{18}O_{LF\text{-}VSMOW}$ values for a variety of natural goethite samples ranging in compositions and textures (Figures 6,7).

5.2. Correcting for matrix effects associated with solid solutions in goethite

As discussed above, a potential source of uncertainty in goethite $\delta^{18}O_{SIMS}$ is the fact that α-FeOOH forms natural solid solutions, where a variety of elements (Al, Mn, Ni, Co, Cu, Cr, V, Ti, etc.) may substitute for Fe^{+3} (Schulze, 1984; Schwertmann, 1994). Variable elemental substitutions and differences in elemental composition between the RM and unknowns may lead to significant instrument fractionation associated with compositionally dependent sputtering efficiency (matrix effects) (Shimizu and Hart, 1982; Ireland, 1995). In addition, natural goethites often contain Si and P as minor elements (Table 1; EA 4,5), and it is unclear whether these elements occur in solid solution or as mineral contaminants (Glasauer and Schwertmann, 1999). Some of the Si may occur as thin films of amorphous silica (opal) coating individual goethite fibers (Glasauer and Schwertmann, 1999); similarly, P may occur as nanofilms of phosphate on crystallite surfaces. These are difficult features to overcome and assess, but they must be factored into matrix corrections.

Figure 2 and Table 1 illustrate the elemental composition of our proposed $\delta^{18}O_{SIMS}$ RM (CL4) and other growth bands (CL1, CL2, and CL5) from the same sample. Table 1 and EA 4,5 show compositions for other natural goethite samples used for calibration purposes. The results show that the goethites investigated in this study contain up to a few percent Al and Si (± Zn, Mn, P, Pb and Cu) as dopants or contaminants. Iron contents are inversely proportional to the concentrations of these elements (Figure 2, Table 1, and EA4,5). This inverse relationship permits using total Fe-contents – or total minor element contents – to correct for compositionally dependent matrix effects on SIMS results, as described in Section 3.7 above and summarized in Figure 3.

We initially assess the suitability of our RM by comparing SIMS and LF results obtained for other Capão goethite growth bands (Figure 2) using CL4 as the reference material. Because other growth bands from the same sample have similar and very negative $\delta^{18}O$ values, share the same texture and mode of precipitation, and only differ slightly in composition, they provide a useful initial test of CL4's performance as a RM. Therefore, using CL4 as RM, we make $\delta^{18}O_{SIMS}$

measurements for CL1, CL2, and CL5 (Figures 2,6). Figure 6b illustrates that CL2 $\delta^{18}O_{SIMS}$ values, corrected for $\alpha_{IMF\text{-}CL4}$ (instrument mass fractionation) only, overlap with its Caltech laser fluorination value, suggesting that CL2 is sufficiently similar to CL4 that compositionally dependent matrix corrections are not required. $^{18}O_{SIMS}$ values for CL1 and CL5, corrected for $\alpha_{IMF\text{-}CL4}$ only (Figures 6 a,c), differ from their laser fluorination results (Caltech values). Figures 6 d,e illustrate $\delta^{18}O_{SIMS}$ measurements for CL1 and CL5, now corrected for both IMF and matrix effects ($\alpha_{IMF\text{-}CL4}$ and α_{matrix}), associated with variable Fe contents ($Bias_{Fe}$) and derived using the run-specific regressions in Figure 3. Figures 6 f,g show the same results corrected for matrix effects associated with all elements (V+Co+P+Cr+Al+Ni+Mn+Si+Pb+Cu+Ti+Zn) potentially replacing Fe in the goethite structure ($Bias_{ALL}$) (regression equations also shown in Figure 3). Both corrections yield IMF- and matrix-corrected $\delta^{18}O_{SIMS}$ measurements very close to their $\delta^{18}O_{LF\text{-}VSMOW}$ values, suggesting that either correction scheme is appropriate.

To assess the same correction schemes applied to goethite samples of different origins, distinct isotopic compositions, and much more varied minor and trace element contents, we repeat the tests above on six additional samples analyzed as calibration goethites: Roy L5, Roy L6, WIN 01B, WIN 03A, BAHLGB, and STOP1-6-D1 (Figure 7). Figure 7 a-f show the measured results using CL4 to correct for IMF only; Figure 7 g-l shows the same results after matrix corrections based on the total Fe contents ($Bias_{Fe}$) (see Figure 3 for regression lines); Figure 7 m-r shows the results matrix corrected using the average contents of all other elements substituting for iron ($Bias_{ALL}$). The plots clearly illustrate that compositionally dependent matrix effects are significant, and that matrix corrections are essential if accurate goethite $\delta^{18}O$ values are to be obtained by SIMS. They also indicate that, for most samples, matrix corrections using total Fe contents or total content of elements substituting for Fe permit reasonably reconciling $\delta^{18}O_{SIMS}$ and $\delta^{18}O_{LF\text{-}VSMOW}$ values. Corrections based on matrix effects associated with all elements replacing Fe may be more appropriate because a decrease in Fe content may not necessarily result in significant matrix corrections. For example, if Fe is replaced by Mn^{3+} in the goethite structure, the matrix effect could potentially be relatively small (this remains to be demonstrated). However, if lowered Fe contents result from the presence of SiO_2 or phosphate nanofilms coating goethite grains, the matrix effect may be significant as $\delta^{18}O$ values in Si-polymorphs or phosphates are generally much more positive (+15-20 ‰) than in goethite. Thus, a matrix correction based on the total amount of the substituting elements, as opposed to a decrease in Fe content, is often more appropriate. And, in fact, $Bias_{ALL}$ does appear to provide a statistically more robust reconciliation (except for sample Roy L5, Figure 7 g,m) between $\delta^{18}O_{SIMS}$ and $\delta^{18}O_{LF\text{-}VSMOW}$ results for most of the runs, justifying preferentially choosing the $Bias_{ALL}$ regressions.

5.3. The effect of crystallographic orientation on $^{18}O/^{16}O$ ratios

Crystallographic orientation is known to affect ionization efficiency during the isotopic analysis of oxides (e.g., hematite, magnetite) by ion microprobes (Lyon et al., 1998; Huberty et al., 2010; Kita et al., 2010). This effect may result in instrument-specific isotopic variability as large as 5 ‰ (magnetite, Lyon et al., 1998) and up to 11 ‰ for the SHRIMP-SI (Llyam White, results on hematite, personal communication), masking potential variations in natural isotopic compositions in these minerals.

Our results reveal a maximum discrepancy of ~ 2 ‰ when goethite samples are analyzed in crystallographic orientations orthogonal to that of RM crystals. Fortuitously, the fact that most goethite grains tend to break into elongated fragments with the direction of elongation parallel to the c-axis ensures that most crystal fragments can be oriented with respect to each other and with respect to the crystallographic orientation of the RM, thus reducing the magnitude of this analytical bias. Therefore, $\delta^{18}O_{SIMS}$ values measured for properly oriented goethite samples should yield much more precise results than those presented here and more faithfully retrieve the mineral's $\delta^{18}O$ value. Despite this caveat, the results in Figure 5b, which illustrate the dispersion of 1027 SHRIMP spot analyses on randomly oriented CL4 crystals, show that, even when grain orientation is unconstrained, relatively precise $\delta^{18}O_{SIMS}$ results are still attainable.

5.4. The effect of porosity on $^{18}O/^{16}O$ ratios

Spot analysis of porous areas in a grain commonly yielded discrepant results from the mean obtained from the analysis of other regions of the same grain. The reoccurrence of this feature in several samples leads to the conclusion that areas of high porosity should be avoided when selecting positions for SHRIMP-SI goethite $^{18}O/^{16}O$ measurements. As porosity is a difficult feature to quantify, it is impossible to ascertain how much of the spread in $\delta^{18}O_{SIMS}$ values within a sample may arise from heterogeneous porosity not readily discernible by visual inspection. Fortunately, porous goethite is yellow, and goethite becomes progressively darker as porosity decreases. Petrographic examination of goethite grains may suffice to determine areas of high porosity to be avoided during SIMS analysis. Porosity is also noticeable by the pitted nature of the reflected-light image of the polished sample in the SHRIMP mount (Figure 8a), another way of screening unsuitably porous samples.

5.5. The influence of texture and multiple generations on the $\delta^{18}O$ values of goethite

Grain BAH-F124-111.2B (Figure 11a) represents a typical colloform goethite symmetrically precipitated from the walls towards the center of an open cavity. After the cavity was completely

sealed by the precipitating goethite (with minor alternating bands of Cu-rich cryptomelane), the sample continued to grow in the direction illustrated by the arrows in Figure 11a. As illustrated in Figure 11a,b, individual growth bands in colloform goethites provide suitable samples for SHRIMP-SI $\delta^{18}O$ analysis: they are well crystallized; the crystals are parallel and elongated along the c-axis avoiding or easily accounting for possible variability related to crystallographic orientation; the results are relatively well constrained and reproducible; the spatial resolution of the SHRIMP-SI resolves the isotopic composition of single bands (too thin to be physically separated and analyzed by other methods); and analyzing individual bands permits detecting changes in the isotopic composition of fluids during mineral precipitation through time, making full use of the advantages provided by in situ analysis with the SIMS.

In contrast, the scatter in $\delta^{18}O_{SIMS}$ values obtained for sample BAH-F124-123.2 may be a function of (a) true variability in the sample, (b) crystallographic orientation (individual crystallites appear to grow aligned in different directions), and (c) porosity, or (d) the combined result of all these effects. These data suggest that sample texture must be used as a vetting criterion for the selection of the best grains or the best areas in a grain to undergo stable isotope analysis with the SHRIMP-SI; however, despite the larger scatter in the $\delta^{18}O_{SIMS}$ data, the $\delta^{18}O_{SIMS}$ values are roughly compatible with the $\delta^{18}O_{LF\text{-}VSMOW}$ result.

6. Application to goethites from an ancient weathering profile in SE Brazil

Here, we illustrate the potential of the methodological approaches refined in this contribution by providing an example that takes advantage of the high-spatial resolution (20-25 μm) of the SHRIMP-SI to measure variations in the oxygen isotope compositions of several generations of intimately intergrown goethites that are too small or too intertwined to be fully resolvable by physical separation. A 3x3x3 cm goethite sample (Figure 12a) from the canga horizon overlying the Gandarela iron deposit, Quadrilátero Ferrífero, Brazil, reveals several generations of intertwined goethite crystals that range in ages from 48.3 ± 4.8 to 9.5 ± 0.9 Ma (n = 52) (Monteiro et al., 2014; 2018), with several apparent ages (mixed ages?) in-between. The results suggest several generations of goethite intergrown at scales not entirely resolvable by methods that require physical separation (e.g., (U-Th)/He geochronology and LF). This intimate intergrowth is confirmed by visual observation of the hand-specimen and by petrographic/SEM analyses (Figure 12). At least four visually distinct generations were identified: a massive and dull reddish-brown goethite (Figure 12b,g); a coarsely-crystalline yellow-orange goethite in veins (Figure 12c,h); a patchy goethite (Figure 12d,h); and a massive and black vitreous goethite (Figure 12e). These four generations were tentatively physically separated and dated. The spread in (U-Th)/He results

(Monteiro et al., 2018) for some of the generations clearly indicates that physically separating each generation is not entirely possible. But average results for each generation (Figure 12) reveal that the dull goethite is the oldest; the yellow veins constitute an intermediate-age generation; the patchy goethite is younger and may reflect a mixture of generations; and the black vitreous goethite is the youngest and isotopically the lightest. The relative ages are consistent with the paragenetic sequences observed in the hand specimen, and thin sections and polished grains (Figure 12). Electron microprobe analysis reveals that the various goethite generations show distinct minor element contents (Figure 12f). Finally, SHRIMP-SI analysis for each generation reveals differences in $\delta^{18}O$ values also.

This complexity in ages, textures, and elemental and isotopic compositions is not resolvable by bulk methods. The high spatial resolution results, however, permit resolving a protracted and complex history of goethite precipitation-dissolution-reprecipitation under contrasting water/rock ratios through time. Weathering of the banded iron-formation and associated quartzites-phyllites in the Quadrilátero Ferrífero initiated sometime prior to ~ 49 Ma under relatively high water/rock ratios ($\delta^{18}O_{goe}$ ~ 0 ‰), promoting the dissolution of Fe- and Al-bearing lithologies, transportation of these elements in solution in the near-surface environment (which suggests the presence of organic acids), and their reprecipitation in duricrusts (canga), forming the 1st-generation Al-rich goethite (Figure 12a-b,g). Its elemental and isotopic compositions suggest that this 1st-generation goethite precipitated under tropical humid conditions with abundant vegetation. The duricrust was stable for a long period, but during the Late Oligocene warming (Zachos et al., 2001), massive influx of meteoric waters promoted partial dissolution of the canga, organic acids helped to leach Al from the system, and a 2nd-generation of goethite, devoid of Al but moderately enriched in Si, precipitated in fractures (Figure 12a,c,h). The low Al contents, light isotopic composition, and abundance of veins of this generation suggest effective flushing by the weathering solutions under high water/rock conditions. This isotopically lighter vein-goethite is consistent with voluminous rainfall (Monteiro, 2018).

The patchy 3rd-generation goethite (Figure 12a, d, h) is isotopically heavy and Al-rich, and its texture, elemental, and isotopic composition suggest fine-scale local partial dissolution-reprecipitation of 1st- and 2nd-generation goethites under relatively low water/rock ratios; re-precipitated goethite masses may contain goethite grains from all generations (1st, 2nd, and 3rd) that are too finely intertwined to be resolved. Partial dissolution of 1st- and 2nd-generation goethite under water-saturated conditions with subsequent precipitation of 3rd-generation goethite by evapotranspiration of weathering solutions during alternating wet-dry climates would account for the textures, heavy isotopic composition, and high Al content of this 3rd-generation goethite.

Finally, massive influx of meteoric water in the Miocene (~11-9 Ma), causing wholesale dissolution-reprecipitation of all previous generations of goethite under high water/rock ratios, led to the formation of 4th-generation vitreous goethite (Figure 12a, e). Dissolution-reprecipitation of goethite occurred in situ, also without flushing of Al from the system. It may record rising groundwater levels, filling of nearby perched lakes, and formation of nearby bauxites by weathering of lake sediments. Interestingly, this last event is coeval with a major regional weathering event in southeastern Brazil retrieved from the Mn oxide $^{40}Ar/^{39}Ar$ record (Carmo and Vasconcelos, 2004; Vasconcelos and Carmo, 2018).

The complexity of the processes above, the coexistence of several generations of goethite in close spatial proximity, and the variability in elemental and isotopic compositions at scales only resolvable by EMPA and with the SHRIMP-SI attest to the benefit of high-spatial resolution methods in the study of supergene minerals. In forthcoming studies, we will illustrate the application of the analytical approaches outlined here to produce time-calibrated paleoprecipitation $\delta^{18}O$ curves for continental weathering profiles in the Amazon and southeastern Brazil to demonstrate that the construction of continental paleoweathering curves complements the paleoclimatic record obtained from ocean sediments.

7. CONCLUSIONS

The Sensitive High Resolution Ion Microprobe for Stable Isotopes (SHRIMP-SI) provides a useful platform for investigating the stable isotope composition preserved in supergene goethites [α-(Fe_{1-x}(Al,Mn,Ni,V,Cu,Co,…)$_x$OOH)] retrieved from continental weathering profiles. Characterization and validation of a suitable reference material (CL4) in this study makes the analysis of goethite by SIMS feasible. Matrix correction procedures, based both on Fe contents, or the abundances of all elements replacing Fe in the goethite structure, permits reconciling SHRIMP-SI and laser fluorination results for the same samples, confirming that texturally appropriate goethite can indeed be accurately analyzed by SIMS. The effects of crystallographic orientation reveal that mounting samples and reference materials in the same crystallographic geometry is the most appropriate approach for ensuring the most precise and accurate results. Sample texture, porosity, and crystallographic characteristics must be used in screening for suitable goethite samples for SHRIMP-SI analyses. The high spatial resolution possible with the ion microprobe permits measuring the isotopic composition of single growth bands in colloform samples, resolving the temporal $\delta^{18}O$ record preserved in natural goethites. It also permits retrieving complex histories of mineral dissolution-reprecipitation often recorded in ancient weathering profiles. If goethites do indeed precipitate at, or near, equilibrium with meteoric

waters, as currently interpreted, $\delta^{18}O_{SIMS}$ analysis permit retrieving the composition of rainwater into the remote past assuming temperatures can be independently retrieved (e.g., Miller, 2018).

Acknowledgements

We thank present and past colleagues from Vale, particularly Carlos Monte Lopes, Luzimar Rego, Clovis Maurity, Paulo Sérgio Ribeiro, Fernando Greco, Fernando Martins, Henrile Meireles, Carlos Augusto de Medeiros Filho, Augusto Kishida, and Felipe Porto for field support in the Carajás region. We thank Carlos Spier, then at MBR, for field support in the Quadrilátero Ferrífero. We thank UQ-CMM staff for help during microanalysis. We thank Mr. Llyam White for carrying additional laser fluorination analyses. This project was funded by the Australian Research Council (ARC Discovery DP160104988) grant to Paulo Vasconcelos and Kenneth Farley, Australian Research Council (ARC LP1401008005) grant to Gordon Southam et al., Australian Research Council (ARC LE0560868) grant to Trevor Ireland, and the Brazilian Research Council (CNPq) Science Without Borders scholarship to Hevelyn Monteiro.

REFERENCES

Bao H. and Koch P. L. (1999) Oxygen isotope fractionation in ferric oxide-water systems: Low temperature synthesis. *Geochimica et Cosmochimica Acta*, **55,** 599-613.

Bao H., Koch P. L. and Thiemens H. (2000) Oxygen isotopic composition of ferric oxides from recent soil, hydrologic, and marine environments. *Geochimica et Cosmochimica Acta*, **64** 2221-2231.

Bird M. I., Longstaffe F. J., Fyfe W. S., and Bildgen P. (1992) Oxygen–isotope systematics in a multiphase weathering system in Haiti. *Geochim. Cosmochim. Acta* **56**, 2831–2838.

Bird M. I., Longstaffe F. J., Fyfe W. S., Kronberg B. I., and Kishida A. (1993) An oxygen-isotope study of weathering in the eastern Amazon Basin, Brazil. In Climate Change in Continental Isotopic Records (ed. P. K. Swart et al.), Vol. 78, pp. 295–307, Geophysical Monograph, American Geophysical Union.

Carmo, I. O. and Vasconcelos, P. M. (2004) Geochronological evidence for pervasive Miocene weathering, Minas Gerais, Brazil. *Earth Surf. Process. Landforms* 29, 1303-1320.

Cornell, R.M., Schwertmann, U. (1996) The iron oxides: structure, properties, reactions, occurrence and uses. Weinheim, New York.

Eiler J. M., Graham C. and Valley J. W. (1997) SIMS analysis of oxygen isotopes: matrix effects in complex minerals and glasses. *Chemical Geology* 138, 221-244.

Girard J.-P., Razanadranorosoa D. and Freyssinet P. (1997) Laser oxygen isotope analysis of weathering goethite from the lateritic profile of Yaou, French Guiana: paleoweathering and paleoclimatic implications. *Applied Geochemistry* 12, 163-174.

Girard J.-P., Freyssinet P., and Chazot G. (2000) Unraveling climatic changes from intraprofile variation in oxygen and hydrogen isotopic composition of goethite and kaolinite in laterites: An integrated study from Yaou, French Guiana. *Geochim. Cosmochim. Acta* **64**, 409–426.

Girard J.-P., Freyssinet P., and Morillon A.-C. (2002) Oxygen isotope study of Cayenne duricrust paleosurfaces: implications for past climate and laterization processes over French Guiana. *Chemical Geology* 191, 329-343.

Glasauer, S., Friedl, J., and Schwertmann, U. (1999) Properties of Goethites Prepared under Acidic and Basic conditions in the Presence of Silicate. *Journal of Colloid and Interface Science* **216**, 106-115.

Heim, J. A. (2006) Geochronology of weathering and landscape evolution, Hamersley Iron Province, Australia, Ph.D. thesis, The University of Queensland, p. 214.

Huberty J. M., Kita N. T., Kozdon R., Heck P. R., Fournelle J. H., Spicuzza M. J., Xu H., and Valley J. W. (2010) Crystal orientation effects in δ18O for magnetite and hematite by SIMS. *Chemical Geology* 276, 269-283.

Ickert R. B., Hiess, J., Williams, I. S., Holden, P., Ireland, T. R., Lanc, P., Schram, N., Foster, J. J., and Clement, S.W. (2008) Determining the high precision, in situ, oxygen isotope ratios with a SHRIMP II: Analyses of MPI-DING silicate-glass reference materials and zircon from contrasting granites. *Chemical Geology* **257**, 114-128.

Ickert R. B. and Stern R. A. Matrix (2013) Corrections and Error Analysis in High Precision SIMS $^{18}O/^{16}O$ Measurements of Ca–Mg–Fe Garnet. *Geostandards and Geoanalytical Research* XX, 1-20.

Ireland T. R. (1995) Ion microprobe mass spectrometry: techniques and applications in cosmochemistry, geochemistry, and geochronology. *Advances in Analytical Geochemistry* **2**, 1-118.

Ireland T. R. (2004) SIMS Measurements of Stable Isotopes. *Handbook of Stable Isotope Analytical Techniques* Volume-I, 654-691

Ireland, T. R., Clement, S., Compston, W., Foster, J. J., Holden, P., Jenkins, B., Lanc, P., Schram, N., and Williams, I. S. (2008) Development of SHRIMP, *Australian Journal of Earth Sciences*, **55**, 937 – 954.

Ireland T.R., Schram N., Holden P., Lanc P., Ávila J., Armstrong R., Amelin Y., Latimore A., Corrigan D., Clement S., Foster J.J., and Compston W. (2014) Charge-mode electrometer measurements of S-isotopic compositions on SHRIMP-SI. International Journal of Mass Spectrometer 359, 26-37.

Kita, N.T., Ushikubo T., Fu B., Valley J. W. (2009) High precision SIMS oxygen isotope analysis and the effect of sample topography. Chemical Geology 264, 43-57

Kita, N.T., Huberty, J.M., Kozdon, R., Beard, B.L., Valley, J.W. (2010) High precision SIMS oxygen, sulphur and iron stable isotope analyses of geological materials: accuracy, surface topography and crystal orientation. Surface and Interface Analysis. Doi:10.1002/sia.3424

Lyon, I. C., Saxton, J.M., Cornah, S.J., 1998. Isotopic fractionation during secondary ionisation mass spectrometry: crystallographic orientation effects in magnetite. International Journal of Mass Spectrometry and Ion Processes 172 (1–2), 115–122.

Martin L. A. J., Rubato D., Crépisson C., Joerg H., Putlitz B., and Vitale-Brovarone A. (2014) Garnet oxygen analysis by SHRIMP-SI: Matrix corrections and application to high-pressure metasomatic rocks from Alpine Corsica, Chemical Geology 374-375, 25-36.

Miller H. B. D., Vasconcelos P. M. P., Eiler J. M., and Farley K. A. (2017) An Australian Cenozoic terrestrial paleoclimate record from He dating and stable isotope geochemistry of goethites. *Geology*, doi: https://doi.org/10.1130/G38989.1.

Miller H. B. D. (2018) Stable and radiogenic isotope studies of iron-oxides as paleoenvironmental and tectonic archives. PhD Thesis. Caltech, 210 p.

Monteiro H. S., Vasconcelos P. M., Farley K. A., Spier C. A. and Mello C. L. (2014) (U-Th)/He geochronology of goethite and the origin and evolution of cangas. *Geochimica et Cosmochimica Acta* **131**, 267-289.

Monteiro H. S. (2017) Paleoenvironmental evolution of continental landscapes through combined high-resolution geochronology and $\delta^{18}O$ ion microprobe analysis of goethite. PhD thesis, The University of Queensland, 376 p.

Monteiro H. S., Vasconcelos P. M., and Farley K. A. (2018) A combined (U-Th)/He and cosmogenic ^{3}He record of landscape armoring by biogeochemical iron cycling. Journal of Geophysical Research: Earth Surface, 123, 298-323. https://doi.org/10.1002/2017JF004282

Mostert A. B. (2014) Variations in Goethite Crystallography with Reference to the Ravensthorpe Ni-Laterite, PhD Thesis, The University of Queensland, Brisbane, p. 290.

Müller, J. (1995) Oxygen isotopes in iron (III) oxides: a new preparation line; mineral-water fractionation factors and paleoenvironmental considerations. Isot. Environ. Health Stud. 31:301-2.

Poage M. A., Sjostrom D. J., Goldberg J., Chamberlain C. P., Furniss G. (2000) Isotopic evidence for Holocene climate change in the northern Rockies from a goethite-rich ferricrete chronosequence. Chemical Geology 166, 327-340.

Schulze, D.G. (1984) The influence of aluminium on iron oxides. VIII. Unit-cell dimensions of Al-substituted goethites and estimation of Al from them. Clays and Clay Minerals 32, 8.

Schwertmann, U. (1994) Aluminum influence on iron oxides: XVII. Unit-cell parameters and aluminium substitution in natural goethites. Soil Science Society of American Journal 58, 256-261.

Shimizu N and Hart S.R. (1982) Applications of the Ion Microprobe to Geochemistry and Cosmochemistry. *Annual Review of Earth and Planetary Sciences*, **10**, 483 526. https://doi.org/10.1146/annurev.ea.10.050182.002411

Sjostrom D. J., Hren M. T. and Chamberlain C. P. (2004) Oxygen isotope records of goethite from ferricrete deposits indicate regionally varying Holocene climate change in the Rocky Mountain region, U.S.A.

Shuster, D. L. (2005) Application of spallogenic noble gases induced by energetic proton irradiation to problems in geochemistry and thermochronometry. Ph.D. thesis, p. 185

Valley, J.W., Kitchen, N., Kohn, M.J., Niendorf, C.R., Spicuzza, M.J. (1995) UWG-2, a garnet standard for oxygen isotope ratios: strategies for high precision and accuracy with laser heating. *Geochimica et Cosmochimica Acta* **59**, 5223–5231.

Vasconcelos P. M., Heim J. A., Farley K. A., Monteiro H. S., Waltenberg K. (2013) $^{40}Ar/^{39}Ar$ and (U-Th)/He - $^{4}He/^{3}He$ geochronology of landscape evolution and channel irondeposit genesis at LynnPeak, Western, Australia. *Geochimica et Cosmochimica Acta* **117**, 283-312.

Vasconcelos P. M. and Carmo I. O. (2018) Calibrating denudation chronology through $^{40}Ar/^{39}Ar$ weathering geochronology. Earth-Science Reviews 179, 411-435.

Vielzeuf D., Champenois M., Valley J. W., Brunet F., and Devidal J. L. (2005) SIMS analyses of oxygen isotopes: Matrix effects in Fe-Mg-Ca garnets. Chemical Geology 223, 208-226.

Waltenberg K. M. (2012). Mineral physics and crystal chemistry of minerals suitable for weathering geochronology: implications to $^{40}Ar/^{39}Ar$ and (U-Th)/He geochronology. PhD Thesis, School of Earth Sciences, The University of Queensland, 421p.

Yang, H., Lu, R., Downs, R.T., Costin, G. (2006) Goethite, a-FeO(OH), from single-crystal data. Acta Crystallographica, Section E: Structure Reports Online E62, i250-i252.

Yapp C. J. (1987) Oxygen and hydrogen isotope variations among goethites (**a**-FeOOH) and the determination of paleotemperatures. Geochim. Cosmochim. Acta 51, 355–364.

Yapp C. J. (1990) Oxygen isotopes in iron(III) oxides. 1. Mineral– water fractionation factors. Chem. Geol. 85, 329–335.

Yapp C. J. (1993) The stable isotope geochemistry of low temperature Fe(III) and Al **"**oxides**"** with implications for continental paleoclimates. Clim. Change Cont. Isotopic Records Geophys. Monograph 78, 285–294.

Yapp C. J. (1997) An assessment of isotopic equilibrium in goethites from a bog iron deposit and a lateritic regolith. Chem. Geol. 135, 159–171.

Yapp C. J. (2000) Climatic implications of surface domains in arrays of **d**D and **d**18O from hydroxyl minerals: goethite as an example. Geochim. Cosmochim. Acta 64, 2009–2025.

Yapp C. J. (2001) Rusty relics of Earth history: iron(III) oxides, isotopes and surficial environments. Ann. Rev. Earth Plan. Sci. 29, 165–199.

Yapp C. J. (2007) Oxygen isotopes in synthetic goethite and a model for the apparent pH dependence of goethite–water $^{18}O/^{16}O$ fractionation. Geochim. Cosmochim. Acta 71, 1115–1129.

Yapp C. J. (2008) $^{18}O/^{16}O$ and D/H in goethite from a North American Oxisol of the Early Eocene climatic optimum. Geochim. Cosmochim. Acta 72, 5838–5851.

Yapp C. J. and Shuster D. L. (2011) Environmental memory and a possible seasonal bias in the stable isotope composition of (UTh)/ He-dated goethite from the Canadian Arctic. Geochim. Cosmochim. Acta 75, 4194–4215.

Yapp, C. J. (2012) Oxygen isotope effects associated with substitution of Al and Fe in synthetic goethite: Some experimental evidence and the criterion of oxygen yield. Geochim. Cosmochim. Acta 97, 200–212.

Zachos, J., Pagani, M., Sloan, L., Thomas, E., and Billups, K. (2000) Trends, Rythms, and Aberrations in Global Climate 65 Ma to Present. Science 292, 686-693.

Zheng, Y-F (1998) Oxygen isotope fractionation between hydroxide minerals and water. Phys. Chem. Mineral. 25:213-21.

List of Tables

Figure Captions

Figure 1. a) SEM image of goethite bands showing µm-size crystals orientated parallel to the direction of growth. b) Goethite grain showing partial dissolution and recrystallization features. Bulk $\delta^{18}O$ analysis will only retrieve average results for these samples. White arrows indicate direction of mineral precipitation. In situ SHRIMP-SI measurement resolves the oxygen isotope composition of each generation, and permits retrieving environmental information for specific periods of mineral precipitation.

Figure 2. (a) A large goethite cobble from a colluvium next to the Capão topaz mine, Minas Gerais, Brazil, displays cm-wide homogeneous colloform bands of nearly stoichiometrically pure $FeOOH_{goe}$, providing a suitable candidate (CL4 RM) for SIMS $\delta^{18}O$ reference material. (b) The inverse relationship between Fe and minor element concentrations suggests that elemental compositions can be used to correct for matrix effects inherent in SIMS methods.

Figure 3. Correlation diagrams between total wt% Fe or total wt% ALL (where ALL = V+Co+P+Cr+Al+Ni+Mn+Si+Pb+Cu+Ti+Zn) against Bias (where Bias = $\delta^{18}O^*_{SIMS}$ - $\delta^{18}O_{LF}$) for the calibration goethite samples analyzed in each SHRIMP-SI run. Fig. 3a, and b illustrate regression curves for the relationships Bias *vs* wt% Fe (a) and Bias *vs* wt% ALL (b), respectively, for all SHRIMP runs together. Fig. 3c, and d show regression lines derived for each separate SHRIMP run. These regressions were used for correcting measured $\delta^{18}O^*_{SIMS}$ results for matrix effects, as discussed in the text.

Figure 4. X-ray diffraction analysis reveals that the sample selected for SHRIMP-SI RM and other natural goethites selected for callibration consist of nearly pure α-FeOOH (lines indicate goethite x-ray diffraction peaks) and are free from significant amounts of contaminants, except for the minor presence of a silica polymorph.

Figure 5. All SHRIMP-SI $\delta^{18}O_{SIMS}$ results obtained for CL4 RM. (a) 294 $\delta^{18}O_{SIMS}$ spot analyses on a large aliquot of CL4 RM, obtained during three different instrument runs, show a natural sample variability of ± 0.5 ‰ (2SD). (b) 1027 $\delta^{18}O_{SIMS}$ spot analysis for several grains of the CL4 RM mounted in different crystallographic orientations shows moderate scatter arising from natural chemical or isotopic heterogeneity and crystal orientation effects. The precision (± 0.7 ‰, 2SD) suggests that CL4 RM constitutes a reasonable SHRIMP-SI reference material.

Figure 6. SHRIMP-SI results for three additional colloform bands (L1, L2, and L5) from the Capão cobble depicted in Figure 2a,c shows that bands L1 and L5 yield uncorrected $\delta^{18}O_{SIMS}$ values that differ from their $\delta^{18}O_{LF\text{-}VSMOW}$ results. Composition-calibrated matrix corrections, using total Fe (Figure 6d,e) or total [V+Co+P+Cr+Al+Ni+Mn+Si+Pb+Cu+Ti+Zn] contents (Figure 6f,g) permit reconciling $\delta^{18}O_{SIMS}$ and $\delta^{18}O_{LF\text{-}VSMOW}$ values. The large scatter for band L5 is consistent with petrographic and XRD data showing that this band has undergone partial recrystallization, goethite crystals are more randomly oriented, and hematite is present. Results for band L2 yield compatible $\delta^{18}O_{SIMS}$ and $\delta^{18}O_{LF\text{-}VSMOW}$ values, suggesting that band L2 probably has similar elemental composition as the CL4 RM.

Figure 7. SHRIMP-SI results for the six relatively pure and well-crystallized goethite samples illustrated in EA1. 7a-f shows that uncorrected $\delta^{18}O_{SIMS}$ values differ significantly from $\delta^{18}O_{LF\text{-}VSMOW}$ results. Composition-calibrated matrix corrections, using total Fe (Figure 7g,l) or total [V+Co+P+Cr+Al+Ni+Mn+Si+Pb+Cu+Ti+Zn] contents (Figure 7m,r) permit reconciling $\delta^{18}O_{SIMS}$ and $\delta^{18}O_{LF\text{-}VSMOW}$ values for all samples. Matrix corrections using total [V+Co+P+Cr+Al+Ni+Mn+Si+Pb+Cu+Ti+Zn] contents permit better reconciliation between SIMS and LF results for all samples except RoyL5 (Figure 6g,m). Errors for each SHRIMP-SI spot analysis were calculated as discussed in the text.

Figure 8. Goethite is orthorhombic and preferentially elongated along the c-axis, and fragments of bands of colloform goethite also fracture elongated along the c-axis. To test the dependency of $\delta^{18}O_{SIMS}$ values on crystal orientation, we analysed two aliquots for sample Winsor 06 01B in distinct crystallographic positions (a-d). The results (d) show a slight difference in measured $\delta^{18}O_{SIMS}$ values for the crystals oriented with the c-axis parallel (a,b) and perpendicularly (c) to the

disk surface. In another experiment (e-h), aliquots of CL4 RM parallel (e,f) or perpendicular (g) to the plane of the page yield the results in (h), revealing a crystal orientation bias of ~ 2‰. In addition to crystal orientation, goethite aliquot in a,d shows that porosity also affects $\delta^{18}O_{SIMS}$ measurements. The porous yellow band (points 5-7 in a,b) yield discrepant results from the rest of the sample, while EMPA does not detect any difference in composition between the yellow and brown bands.

Figure 9: SHRIMP-SI results obtained for three aliquots of the CL4 RM (analysed as unknowns), where the aliquots have b-axes parallel to the disk surface (c). With the disk oriented as shown in (a), the three crystal fragments in (d) were analyzed, yielding the results shown in f. When the disk is rotated 90° clockwise and reanalyzed (b,e), the results show larger discrepancies between $\delta^{18}O_{SIMS}$ and $\delta^{18}O_{LF\text{-}VSMOW}$ values.

Figure 10: Fragments of pressed pellets of synthetic goethite yield the $\delta^{18}O_{SIMS}$ numerical results shown in yellow. The scattered results prevent the use of these synthetic samples as SHRIMP-SI $\delta^{18}O_{SIMS}$ goethite reference materials. However, despite the large scatter, the data (e.g., goethite precipitated at pH>12 shows progressively lighter isotopic composition with temperature, while goethites precipitated at the same temperature but at pH<2 show heavier $\delta^{18}O$ values) suggest that broad trends in $\delta^{18}O_{SIMS}$ values for synthetic samples may be resolved with the SHRIMP-SI, even if precision is partially compromised by sample porosity.

Figure 11: (a, b) Repeatability of SHRIMP-SI $\delta^{18}O$ results for symmetrical colloform bands on opposite walls of a cavity infilled with goethite (white arrows indicate direction of crystal growth). The entire population yields a relatively narrow $\delta^{18}O_{SIMS}$ range (0.3 ± 0.6 ‰ (1SD)) compatible with its $\delta^{18}O_{LF\text{-}VSMOW}$ value of 0.4 ± 0.2 ‰ (1SD). Figure 11c,d illustrates the repeatability of SHRIMP-SI $\delta^{18}O$ results for an optically homogeneous goethite sample. Figure 11e,f show much larger scatter in $\delta^{18}O_{SIMS}$ results when goethite masses comprise randomly oriented and poorly packed crystals.

Figure 12. (a) Hand-specimen of several generations of goethite cementing a canga horizon in the Gandarela plateau, Minas Gerais, Brazil (Monteiro et al., 2014; 2018). The results reveal that the Al-rich first-generation (48-?? Ma?) goethite has a ~$\delta^{18}O_{SIMS}$ value of -0.3 ± 0.2 ‰; it is cross-cut by isotopically light ($\delta^{18}O_{SIMS}$ = -1.2 ± 0.6 ‰) and Si-rich/Al-poor second generation (~27±6 Ma) goethite; patchy goethite is also Al-rich, isotopically heavy (~$\delta^{18}O_{SIMS}$ value of 3.4 ± 0.5 ‰), and young (18.7 ± 1.8 Ma, n=6); and pure vitreous goethite is the youngest (11.3 ± 1.1 Ma, n=6) and isotopically the lightest ($\delta^{18}O_{SIMS}$ = -1.4 ± 0.3 ‰). These complex textures and distributions of

ages, chemical and isotopic compositions record important episodes of the weathering history for the Quadrilátero Ferrífero, Brazil, in one 3x3x3 cm hand specimen.

Table 1: Elemental composition of all goethite samples.

	Capao -L4	**± *(1 σ)***	**Capao -L1**	**± *(1 σ)***	**Capao -L5**	**± *(1 σ)***	**Roy-L5**	**± *(1 σ)***	**Roy-L6**	**± *(1 σ)***	**Win-01B**	**± *(1 σ)***	**Win-03A(*)**	**± *(1 σ)***	**Stop-1-6-D1**	**± *(1 σ)***	**BAH LGB**	**± *(1 σ)***
Element	n = 37		n = 20		n = 8		n = 6		n = 6		n = 30		n = 11		n = 28		n = 53	
O	35.78	*0.90*	35.76	*0.75*	37.64	*0.51*	37.44	*0.67*	37.59	*0.51*	36.99	*0.39*	37.76	*0.49*	37.73	*0.61*	36.17	*0.89*
Na	0.01	*0.05*	0.01	*0.01*	0.02	*0.02*	0.04	*0.04*	0.02	*0.02*	0.02	*0.02*	0.00	*0.01*	0.07	*0.06*	0.01	*0.02*
K	0.00	*0.01*	0.01	*0.01*	0.00	*0.00*	0.01	*0.01*	0.00	*0.00*	0.01	*0.01*	0.02	*0.05*	0.00	*0.00*	0.01	*0.01*
V	0.00	*0.02*	0.02	*0.03*	0.02	*0.03*	0.00	*0.00*	0.01	*0.02*	-		0.03	*0.06*	0.01	*0.02*	0.01	*0.02*
Co	0.07	*0.02*	0.08	*0.04*	0.09	*0.05*	0.05	*0.02*	0.06	*0.01*	0.08	*0.03*	0.07	*0.03*	0.00	*0.02*	0.07	*0.03*
Mg	0.11	*0.02*	0.11	*0.03*	0.30	*0.04*	0.02	*0.01*	0.00	*0.00*	0.05	*0.03*	0.16	*0.18*	0.16	*0.01*	0.04	*0.05*
P	0.02	*0.03*	0.01	*0.01*	0.02	*0.01*	0.01	*0.01*	0.02	*0.01*	0.05	*0.02*	0.26	*0.13*	0.76	*0.17*	0.09	*0.05*
Cr	0.01	*0.01*	0.01	*0.02*	0.00	*0.01*	0.00	*0.01*	0.01	*0.01*	0.01	*0.02*	0.00	*0.01*	0.00	*0.01*	0.01	*0.02*
Fe	61.21	*0.77*	62.64	*1.02*	58.64	*0.33*	60.04	*0.57*	60.65	*0.53*	62.41	*0.43*	58.02	*1.58*	58.44	*1.43*	61.84	*1.54*
Al	0.12	*0.02*	0.15	*0.03*	0.32	*0.06*	0.11	*0.02*	0.13	*0.01*	0.12	*0.04*	0.34	*0.21*	0.02	*0.05*	0.14	*0.05*
S	0.03	*0.10*	0.02	*0.02*	0.02	*0.01*	0.03	*0.01*	0.01	*0.01*	0.02	*0.01*	0.01	*0.01*	0.01	*0.01*	0.01	*0.01*
Ni	0.01	*0.02*	0.01	*0.02*	0.01	*0.01*	0.00	*0.00*	0.00	*0.00*	0.01	*0.02*	0.02	*0.03*	0.00	*0.01*	0.01	*0.02*
Mn	0.05	*0.02*	0.05	*0.03*	0.10	*0.03*	0.55	*0.04*	0.62	*0.05*	0.25	*0.05*	0.21	*0.14*	0.09	*0.02*	0.08	*0.06*
Si	1.12	*0.09*	0.71	*0.22*	1.81	*0.10*	1.08	*0.06*	1.08	*0.04*	0.98	*0.13*	1.59	*0.61*	1.37	*0.31*	1.35	*0.24*
Pb	0.26	*0.06*	0.22	*0.09*	0.24	*0.07*	0.02	*0.02*	0.02	*0.03*	0.04	*0.03*	0.05	*0.05*	0.00	*0.03*	0.10	*0.11*
Cu	0.02	*0.03*	0.03	*0.02*	0.10	*0.03*	0.01	*0.01*	0.00	*0.00*	0.02	*0.02*	0.14	*0.18*	0.00	*0.01*	0.14	*0.09*
Ti	0.00	*0.02*	0.02	*0.02*	0.01	*0.02*	0.03	*0.02*	0.01	*0.01*	0.02	*0.03*	0.02	*0.03*	0.00	*0.01*	0.01	*0.02*
Ca	0.00	*0.03*	0.00	*0.00*	0.05	*0.01*	0.00	*0.00*	0.00	*0.00*	0.07	*0.22*	0.11	*0.14*	0.20	*0.06*	0.00	*0.00*
Zn	0.03	*0.04*	0.02	*0.04*	0.04	*0.03*	0.01	*0.01*	0.03	*0.02*	0.01	*0.04*	0.38	*0.14*	0.02	*0.02*	0.02	*0.03*
Ba	-		0.02	*0.02*	0.02	*0.02*	-		-		0.04	*0.04*	0.03	*0.03*	-		0.03	*0.04*
Sr	-		0.02	*0.02*	0.00	*0.01*	-		-		0.01	*0.01*	-		-		0.02	*0.02*
Cl	-				-		-		-		-		0.01	*0.01*	-			

Total	98.83	*1.03*	99.90	*1.04*	99.45	*0.50*	99.44	*0.91*	100.25	*0.79*	101.21	*0.53*	99.25	*0.69*	98.88	*1.38*	100.15	*1.21*

(*) Data from Waltenberg (2012)

Table 2

Capao L5	261.1	7.2	1.85	0.04	0.08	0.02	2.75	0.13	0.04
Average	***227.0***		***2.0***		***0.1***		***2.5***		***0.03***
S.D. (1σ)	***19.9***		***0.3***		***0.0***		***0.3***		
Win 01B	209.7	4.5	8.10	0.06	0.08	0.02	9.47	0.39	0.01
Win 01B	202.6	4.5	8.04	0.08	0.07	0.02	9.08	0.29	0.01
Win 01B	202.9	4.3	7.94	0.06	0.04	0.02	8.97	0.37	0.01
Win 01B	203.5	4.7	7.94	0.09	0.18	0.03	9.03	0.24	0.02
Win 01B	187.1	4.4	7.85	0.09	0.09	0.03	8.17	0.21	0.01
Average	***201.1***		***8.0***		***0.1***		***8.9***		***0.01***
S.D. (1σ)	***8.4***		***0.1***		***0.1***		***0.5***		
Roy L5	66.6	1.8	3.18	0.06	0.21	0.02	1.18	0.04	0.07
Roy L5	67.5	1.9	3.24	0.06	0.30	0.03	1.22	0.03	0.09
Average	***67.1***		***3.2***		***0.3***		***1.2***		***0.08***
S.D. (1σ)	***0.7***		***0.0***		***0.1***		***0.0***		
Roy L6	78.9	2.0	3.66	0.06	0.12	0.02	1.59	0.06	0.03
Roy L6	77.9	2.2	3.52	0.07	0.13	0.03	1.52	0.03	0.04

Average	***78.4***		***3.6***		***0.1***		***1.6***		***0.03***
S.D. (1σ)	***0.7***		***0.1***		***0.0***		***0.1***		
WIN 03A(b)*	37.7	-	150.48	-	8.96	-	31.34	-	0.06
WIN 03A(c)*	37.8	-	150.53	-	2.71	-	31.13	-	0.02
WIN 03A(d)*	36.8	-	317.35	-	18.24	-	64.61	-	0.06
Average	***37.4***		***206.1***		***10.0***		***42.4***		***0.05***
S.D. (1σ)	***0.5***		***96.3***		***7.8***		***19.3***		
BAHLGB	16.9	0.3	75.4	0.3	0.05	0.02	6.3	0.2	0.001
BAHLGB	15.6	0.3	81.7	0.3	0.06	0.02	6.3	0.3	0.001
Average	***16.3***		***78.5***		***0.1***		***6.3***		***0.00***
S.D. (1σ)	***0.9***		***4.5***		***0.0***		***0.0***		
STOP1-6-D1‡	2.8	0.2	3.11	-	0.21	-	0.05	-	0.07
STOP1-6-D1‡	4.1	0.2	3.33	-	0.11	-	0.08	-	0.03
Average	***3.5***		***3.2***		***0.2***		***0.1***		***0.05***
S.D. (1σ)	***0.9***		***0.2***		***0.1***		***0.0***		

not used to calculate the average

* He age from Waltenberg (2012)

‡ He age from Heim (2006)

Table 3: Laser fluorination $\delta^{18}O$ results

Sample	Mass (mg)	yield (%)	$\delta^{18}O_{VSMOW}$ (‰)	± 1σ	Laboratory

CL1	1.59	54		-18.083	0.033	1
	2.05	89		-18.076	0.033	1
			Average	**-18.079**		
			1sd	0.005		
		99		-17.21	0.20	2
CL2	1.04	97		**-17.90**	0.01	1
	1.67	99		-16.31	0.20	2
CL4	1.11	100		-17.22	0.03	1
	1.84	106		-17.72	0.05	1
	1.93	111		-17.27	0.02	1
	1.58	109		-16.90	0.05	1
	1.81	107		-17.34	0.02	1
			Average	**-17.29**		
			1sd	0.29		
		104		-16.34	0.20	2
		99		-16.33	0.20	2
CL5	1.38	94		**-16.19**	0.03	1
Roy L5	1.84	112		-1.41	0.02	1
	2.07	110		-1.33	0.02	1
	2.68	110		-1.27	0.04	1
	1.55	111		-1.36	0.09	1
	2.15	92		-1.41	0.20	2
			Average	**-1.36**		
			1sd	0.06		

Roy L6	1.65	115		-0.94	0.03	1
	1.81	115		-1.19	0.03	1
	2.37	111		-1.14	0.07	1
	1.99	109		-1.38	0.07	1
	1.92	110		-1.19	0.20	2
			Average	**-1.17**		
			1sd	0.16		
Win 01B	1.84	37		-13.64	0.03	1
	1.50	99		**-12.20**	0.20	2
Win 03A	1.73	108		-2.21	0.02	1
	1.96	110		-1.96	0.20	2
			Average	**-2.08**		
			1sd	0.18		
BAHLGB	1.62	108		-2.68	0.02	1
	1.55	84		-2.52	0.20	2
			Average	**-2.60**		
			1sd	0.12		
Stop1-6-D1	1.60	106		**-0.67**	0.04	1

(bold): $\delta^{18}O$ value used for matrix calibration

1: Caltech

2: University of Oregon

Table 4: Summary of SHRIMP-SI oxygen isotope ratios and uncertainties. RM = reference material.

Run	Session	$\delta^{18}O_{SIMS}$	± Internal $error_{sample}$ (95% CI)	Standard deviation (1σ)	Standard Error of the Mean (95% CI)	MSWD	± External error (1σ)	no. spots	no. outliers	$\delta^{18}O_{VSMOW}$	$Bias_{ME}$ (*)	$Bias_{Fe}$	$Bias_{ALL}$	$\delta^{18}O_{SIMS}$ (corrected-Fe)	$\delta^{18}O_{SIMS}$ (corrected-ALL)
R2	**HM-1**														
	CL4 - normalizing RM	**-17.3**	**0.2**	**0.1**	**0.2**	**0.8**	**0.2**	**4**	**0**	**-17.3**	-				
	CL1	-18.3	0.3	0.3		0.4	0.3	4	0	-18.1	-0.2	-0.4	-0.7	-17.9	-17.6
	CL1	-19.3	0.7	0.2		6.3	0.5	7	4	-18.1	-1.2	-0.4	-0.7	-18.9	-18.6
	CL2	-19.5	0.1	0.2		1.6	0.1	10	3	-17.9	-1.6				
	CL5	-14.6	0.5	0.5		14.2	0.5	7	0	-16.2	1.6	2.3	2.3	-16.8	-16.8
	CL5	-12.9	0.4	0.3		4.2	0.4	6	1	-16.2	3.3	2.3	2.3	-15.2	-15.2
	Win 01B	-11.7	0.2	0.2		0.6	0.2	9	3	-12.2	0.5	-0.2	-0.1	-11.5	-11.6
	Win 01B	-12.2	0.3	0.3		5.4	0.3	6	0	-12.2	0.0	-0.2	-0.1	-12.0	-12.1
	BAH	-1.7	1.4	0.1		0.1	1.0	2	0	-2.6	0.9	0.1	0.8	-1.9	-2.5
	BAH	-1.6	0.2	0.3		2.0	0.3	9	0	-2.6	1.0	0.1	0.8	-1.7	-2.3
R2	**HM-4**														
	CL4 - normalizing RM	**-17.3**	**0.1**	**0.3**	**0.1**	**2.0**	**0.2**	**19**	**0**	**-17.3**	-				
	CL1	-17.4	0.3	0.1		0.2	0.2	4	0	-18.1	0.7	-0.4	-0.7	-17.0	-16.7
	CL1	-19.3	0.6	0.2		1.2	0.4	3	3	-18.1	-1.2	-0.4	-0.7	-18.5	-18.2
	CL1	-19.4	0.9	0.4		5.3	0.7	5	2	-18.1	-1.3	-0.4	-0.7	-18.5	-18.2
	CL2	-16.2	0.4	0.5		5.4	0.4	7	0	-17.9	1.7				
	CL2	-17.8	0.3	0.2		1.1	0.3	3	0	-17.9	0.1				
	CL5	-12.5	0.2	0.2		0.9	0.2	7	0	-16.2	3.7	2.3	2.3	-14.7	-14.8
	CL5	-11.9	0.5	0.2		2.5	0.4	3	0	-16.2	4.3	2.3	2.3	-14.1	-14.2

	CL5	-14.6	0.3	0.3		1.9	0.3	5	0	-16.2	1.6	2.3	2.3	-16.8	-16.9
	CL5	-15.0	0.4	0.2		0.8	0.3	4	0	-16.2	1.2	2.3	2.3	-17.3	-17.3
	CL5	-15.4	0.6	0.3		4.8	0.4	6	2	-16.2	0.8	2.3	2.3	-17.7	-17.7
	Win 01B	-12.9	1.2	0.5		11.9	0.9	4	1	-12.2	-0.7	-0.2	-0.1	-12.7	-12.8
	Win 01B	-12.0	1.1	0.8		8.9	0.9	4	0	-12.2	0.2	-0.2	-0.1	-11.7	-11.9
	BAH	-2.5	0.8	0.3		2.9	0.6	3	0	-2.6	0.1	0.1	0.8	-2.6	-3.2
R4	**JA-1**														
	CL4 - normalizing RM	**-17.3**	**0.1**	**0.3**	**0.1**	**3.8**	**0.3**	**63**	**1**	**-17.3**	**-**				
	CL2	-17.9	0.2	0.2		1.1	0.2	9	1	-17.9	0.0				
	CL2	-18.9	0.3	0.3		3.4	0.3	8	0	-17.9	-1.0				
	CL2	-17.8	0.4	0.4		4.9	0.4	8	0	-17.9	0.1				
	CL2	-18.8	0.1	0.2		0.6	0.1	8	0	-17.9	-0.9				
	CL2	-18.2	0.2	0.2		2.3	0.2	8	0	-17.9	-0.3				
	CL2	-17.4	0.4	0.5		5.2	0.4	8	1	-17.9	0.5				
	CL2	-16.0	0.3	0.4		7.1	0.3	8	0	-17.9	1.9				
	CL2	-17.6	0.2	0.2		0.6	0.2	6	0	-17.9	0.3				
	CL2	-17.4	0.2	0.3		2.1	0.2	8	0	-17.9	0.5				
	CL2	-19.0	0.2	0.2		2.0	0.2	8	5	-17.9	-1.1				
R5	**HM-13**														
	CL4 - normalizing RM	**-17.3**	**0.3**	**0.6**	**0.3**	**9.1**	**0.5**	**18**	**1**	**-17.3**	**-**				
	Win 01B	-11.1	0.7	0.3		2.1	0.5	4	1	-12.2	1.1	0.3	0.6	-11.4	-11.7
	Win 01B	-12.3	0.6	0.7		14.5	0.6	8	0	-12.2	-0.1	0.3	0.6	-12.6	-13.0
	Win 03A	0.6	0.4	0.3		1.2	0.3	3	0	-2.1	2.7	2.3	2.8	-1.6	-2.2
	Win 03A	0.5	2.2	0.3		1.6	1.6	3	1	-2.1	2.6	2.3	2.8	-1.8	-2.4
	Roy L5	0.1	0.4	0.1		0.3	0.3	5	2	-1.4	1.5	1.4	1.0	-1.3	-0.9

	Roy L5	0.0	0.4	0.1		0.8	0.3	3	0	-1.4	1.3	1.4	1.0	-1.4	-1.0
	Roy L5	-0.1	0.5	0.2		1.3	0.4	4	1	-1.4	1.3	1.4	1.0	-1.4	-1.1
	Roy L6	0.7	0.4	0.1		0.5	0.3	3	0	-1.2	1.8	1.1	1.2	-0.4	-0.5
	Roy L6	0.6	0.4	0.2		0.8	0.3	5	2	-1.2	1.8	1.1	1.2	-0.5	-0.6
	Roy L6	1.2	4.4	0.5		4.6	3.1	2	0	-1.2	2.4	1.1	1.2	0.1	0.0
	Roy L6	0.6	2.0	0.2		1.3	1.5	2	0	-1.2	1.8	1.1	1.2	-0.5	-0.6
	Stop1-6-D1	0.9	0.5	0.5		9.2	0.5	6	0	-0.7	1.6	2.1	1.6	-1.2	-0.7
	Stop1-6-D1	1.1	0.9	0.4		5.5	0.7	3	0	-0.7	1.8	2.1	1.6	-1.0	-0.5
	Stop1-6-D1	1.1	1.1	0.4		6.2	0.8	4	1	-0.7	1.8	2.1	1.6	-1.0	-0.5
	Stop1-6-D1	0.6	0.4	0.0		0.1	0.3	3	0	-0.7	1.2	2.1	1.6	-1.5	-1.0
R5	**HM-15**														
	CL4 - normalizing RM	**-17.3**	**0.1**	**0.3**	**0.1**	**2.5**	**0.2**	**21**	**3**	**-17.3**	**-**				
R5	**HM-16_TH**														
	CL4 - normalizing RM	**-17.3**	**0.2**	**0.4**	**0.2**	**3.8**	**0.3**	**14**	**0**	**-17.3**	**-**				
R6	**HM-19_HM-20**														
	CL4 - normalizing RM	**-17.3**	**0.2**	**0.6**	**0.1**	**23.1**	**0.4**	**58**	0	**-17.3**	**-**				
	Roy L5	1.5	0.3	0.2		3.7	0.3	5	0	-1.4	2.9	2.7	2.1	-1.2	-0.6
	Roy L5	2.1	0.3	0.4		4.3	0.4	9	1	-1.4	3.4	2.7	2.1	-0.7	0.0
	Roy L5	3.5	0.3	0.2		3.7	0.3	5	0	-1.4	4.8	2.7	2.1	0.7	1.3
	Roy L6	2.5	0.2	0.2		2.3	0.2	8	1	-1.2	3.7	2.0	2.9	0.5	-0.4
	Roy L6	2.1	0.2	0.2		1.7	0.2	12	1	-1.2	3.2	2.0	2.9	0.1	-0.8
	Roy L6	1.6	0.3	0.2		1.5	0.2	5	1	-1.2	2.8	2.0	2.9	-0.4	-1.2
	Stop1-6-D1	3.2	0.2	0.2		1.6	0.2	6	0	-0.7	3.9	4.7	4.7	-1.5	-1.5

	Stop1-6-D1	3.1	0.4	0.4		7.5	0.4	7	1	-0.7	3.8	4.7	4.7	-1.6	-1.5
	Stop1-6-D1	3.2	0.5	0.2		2.9	0.4	3	0	-0.7	3.9	4.7	4.7	-1.5	-1.4
R6	**HM-20_BAH**														
	CL4 - normalizing RM	**-17.3**	**0.1**	**0.3**	**0.1**	**5.0**	**0.3**	**36**	**4**	**-17.3**	**-**				
	Roy L5	0.4	0.4	0.3		3.1	0.3	4	0	-1.4	1.7	2.7	2.1	-2.4	-1.7
	Roy L5	1.1	0.2	0.2		0.8	0.2	5	0	-1.4	2.4	2.7	2.1	-1.7	-1.0
	Roy L5	1.3	1.0	0.7		13.2	0.9	5	1	-1.4	2.7	2.7	2.1	-1.4	-0.8
	Roy L5	2.8	0.2	0.1		1.0	0.1	5	1	-1.4	4.1	2.7	2.1	0.0	0.7
	Roy L6	2.9	0.6	0.3		6.1	0.5	4	0	-1.2	4.1	2.0	2.9	0.9	0.1
	Roy L6	2.6	0.5	0.5		15.9	0.5	6	0	-1.2	3.8	2.0	2.9	0.6	-0.3
	Roy L6	2.8	0.7	0.6		19.8	0.7	5	0	-1.2	4.0	2.0	2.9	0.8	0.0
	Roy L6	2.0	0.5	0.4		10.0	0.5	5	0	-1.2	3.2	2.0	2.9	0.0	-0.8
	Stop1-6-D1	2.9	0.3	0.2		1.2	0.3	4	0	-0.7	3.6	4.7	4.7	-1.8	-1.8
	Stop1-6-D1	3.1	0.2	0.2		2.2	0.2	5	0	-0.7	3.7	4.7	4.7	-1.6	-1.6
	Stop1-6-D1	2.6	0.5	0.4		9.4	0.5	5	0	-0.7	3.2	4.7	4.7	-2.1	-2.1
	Stop1-6-D1	3.4	0.3	0.2		3.4	0.3	5	0	-0.7	4.1	4.7	4.7	-1.3	-1.3
R7	**HM-17**														
	CL4 - normalizing RM	**-17.3**	**0.2**	**0.4**	**0.1**	**7.2**	**0.3**	**53**	**3**	**-17.3**	**-**				
	Roy L5	2.1	2.0	0.7		34.2	1.5	4	1	-1.4	3.4	2.3	1.9	-0.2	0.2
	Roy L5	2.4	0.4	0.3		7.0	0.3	7	1	-1.4	3.7	2.3	1.9	0.1	0.4
	Roy L5	2.3	1.1	0.5		7.5	0.9	4	1	-1.4	3.7	2.3	1.9	0.0	0.4
	Roy L6	1.9	0.4	0.5		4.6	0.4	7	0	-1.2	3.0	1.9	2.1	-0.1	-0.3
	Roy L6	3.1	0.7	0.2		3.5	0.5	3	0	-1.2	4.3	1.9	2.1	1.2	1.0
	Roy L6	2.7	0.4	0.0		0.0	0.3	4	1	-1.2	3.9	1.9	2.1	0.8	0.6

R7	**HM-17-D**														
	CL4 - normalizing RM	**-17.3**	**0.2**	**0.5**	**0.2**	**9.0**	**0.4**	**44**	**4**	**-17.3**	**-**				
	Roy L5	0.9	0.7	0.9		32.1	0.8	10	0	-1.4	2.3	2.3	1.9	-1.4	-1.0
	Roy L5	1.3	0.7	0.6		4.2	0.7	5	0	-1.4	2.7	2.3	1.9	-1.0	-0.6
	Roy L6	1.8	0.2	0.3		0.7	0.3	9	1	-1.2	3.0	1.9	2.1	-0.1	-0.3
	Roy L6	1.7	1.4	0.5		2.1	1.0	3	0	-1.2	2.9	1.9	2.1	-0.2	-0.4
	BAH	0.1	0.9	0.5		10.0	0.7	5	1	-2.6	2.7	3.3	2.6	-3.2	-2.5
	BAH	0.1	0.8	0.5		5.3	0.7	4	0	-2.6	2.7	3.3	2.6	-3.2	-2.6
R7	**HM-21**														
	CL4 - normalizing RM	**-17.3**	**0.1**	**0.4**	**0.1**	**4.5**	**0.3**	**41**	**3**	**-17.3**	**-**				
	Roy L5	1.7	0.4	0.6		9.9	0.5	13	3	-1.4	3.1	2.3	1.9	-0.6	-0.2
	Roy L6	1.0	0.3	0.5		2.7	0.5	12	4	-1.2	2.1	1.9	2.1	-1.0	-1.1
	Stop1-6-D1	2.1	0.2	0.2		1.5	0.2	11	4	-0.7	2.8	3.3	2.6	-1.1	-0.5
R7	**HM-23**														
	CL4 - normalizing RM	**-17.3**	**0.2**	**0.6**	**0.2**	**11.2**	**0.4**	**40**	**2**	**-17.3**	**-**				
	Win 03A	1.8	0.2	0.4		4.0	0.3	16	2	-2.1	3.9	3.5	4.1	-1.7	-2.3
	Win 03A	1.7	0.2	0.4		4.7	0.3	14	3	-2.1	3.8	3.5	4.1	-2.4	-2.3
	Roy L5	1.8	0.2	0.4		9.1	0.3	16	1	-1.4	3.1	2.3	1.9	-0.5	-0.2
	Roy L5	0.7	0.4	0.4		4.6	0.4	8	1	-1.4	2.0	2.3	1.9	-1.6	-1.3
	Roy L6	1.9	0.2	0.4		4.1	0.3	16	2	-1.2	3.0	1.9	2.1	-0.1	-0.2
	Roy L6	0.7	0.5	0.6		8.0	0.5	8	1	-1.2	1.9	1.9	2.1	-1.2	-1.4
R7	**HM-23B**														
	CL4 - normalizing RM	**-17.3**	**0.4**	**0.4**	**0.3**	**6.7**	**0.4**	**8**	**1**	**-17.3**	**-**				

	Win 03A	2.2	1.7	0.8		7.3	1.3	3	0	-2.1	4.3	3.5	4.1	-1.3	-1.9
	Win 03A	2.2	0.8	0.3		1.6	0.6	3	0	-2.1	4.3	3.5	4.1	-2.2	-2.2
	Roy L5	1.3	1.7	0.0		0.0	1.2	3	1	-1.4	2.7	2.3	1.9	-1.0	-0.6
	Roy L5	0.1	0.6	0.1		0.2	0.4	3	0	-1.4	1.4	2.3	1.9	-2.2	-1.8
	Roy L6	1.3	3.1	0.3		4.3	2.2	3	1	-1.2	2.5	1.9	2.1	-0.6	-0.8
	Roy L6	0.1	2.6	0.2		0.4	1.8	3	1	-1.2	1.3	1.9	2.1	-1.8	-2.0
R7	**HM-23_HM-27**														
	CL4 - normalizing RM	**-17.3**	**0.1**	**0.4**	**0.1**	**2.4**	**0.3**	**28**	**3**	**-17.3**	**-**				
	CL1	-16.8	0.2	0.3		2.0	0.2	10	2	-18.1	1.3	0.7	1.0	-17.5	-17.7
	CL2	-17.8	0.2	0.3		3.4	0.3	10	2	-17.9	0.1				
	Win 03A	1.8	1.2	0.5		5.3	0.9	4	1	-2.1	3.9	3.5	4.1	-1.7	-2.3
	Win 03A	1.8	0.3	0.2		0.9	0.3	4	0	-2.1	3.8	3.5	4.1	-1.8	-2.4
	Roy L5	1.4	0.9	0.7		5.1	0.8	6	2	-1.4	2.7	2.3	1.9	-0.9	-0.5
	Roy L5	0.4	0.3	0.1		0.4	0.2	5	1	-1.4	1.8	2.3	1.9	-1.9	-1.5
	Roy L6	2.1	0.8	0.5		13.1	0.7	4	0	-1.2	3.2	1.9	2.1	0.1	0.0
	Roy L6	0.8	0.6	0.4		2.6	0.5	4	0	-1.2	1.9	1.9	2.1	-1.2	-1.4
R7	**HM-23**														
	CL4 - normalizing RM	**-17.3**	**0.2**	**0.4**	**0.2**	**5.8**	**0.3**	**31**	**3**	**-17.3**	**-**				
	Win 03A	2.0	0.2	0.3		1.4	0.2	9	2	-2.1	4.0	3.5	4.1	-1.6	-2.2
	Win 03A	2.3	0.3	0.3		3.3	0.3	10	0	-2.1	4.3	3.5	4.1	-1.3	-1.9
	Roy L5	1.8	0.5	0.5		5.2	0.5	6	0	-1.4	3.2	2.3	1.9	-0.5	-0.1
	Roy L5	-0.3	0.4	0.4		3.5	0.4	5	1	-1.4	1.1	2.3	1.9	-2.6	-2.2
	Roy L6	1.7	0.6	0.6		4.6	0.6	5	1	-1.2	2.9	1.9	2.1	-0.2	-0.4
	Roy L6	0.9	0.2	0.3		1.3	0.3	7	2	-1.2	2.0	1.9	2.1	-1.1	-1.3

R8	**HM-22_JA**														
	CL4 - normalizing RM	**-17.3**	**0.1**	**0.4**	**0.1**	**10.8**	**0.3**	**57**	**0**	**-17.3**	**-**				
	Roy L5	-1.0	0.2	0.3		5.2	0.3	11	1	-1.4	0.3	0.4	0.1	-1.5	-1.2
	Roy L6	-0.9	0.3	0.6		13.8	0.5	11	1	-1.2	0.3	0.3	0.2	-1.1	-1.1
R8	**HM-BAH_JA**														
	CL4 - normalizing RM	**-17.3**	**0.1**	**0.3**	**0.1**	**6.0**	**0.2**	**48**	**0**	**-17.3**	**-**				
	BAH	-2.4	0.1	0.3		5.4	0.2	20	1	-2.6	0.2	0.9	0.4	-3.3	-2.8
R8	**HM-23_JA**														
	CL4 - normalizing RM	**-17.3**	**0.1**	**0.3**	**0.1**	**6.8**	**0.2**	**37**	**1**	**-17.3**	**-**				
	Win 03A	-0.5	0.2	0.2		3.7	0.2	10	0	-2.1	1.6	1.0	1.1	-1.5	-1.6
	Win 03A	-1.5	0.4	0.4		10.3	0.4	8	1	-2.1	0.6	1.0	1.1	-2.4	-2.5
	Roy L6	-1.9	0.4	0.5		13.5	0.5	11	1	-1.2	-0.7	0.3	0.2	-2.2	-2.1
	Roy L6	-0.5	0.2	0.3		6.5	0.3	11	1	-1.2	0.7	0.3	0.2	-0.7	-0.7
R8	**HM-22**														
	CL4 - normalizing RM	**-17.3**	**0.1**	**0.3**	**0.3**	**2.6**	**0.2**	**7**	**0**	**-17.3**	**-**				
R9	**HM-27_HM-16**														
	CL4 - normalizing RM	**-17.3**	**0.1**	**0.3**	**0.1**	**5.6**	**0.2**	**64**	**0**	**-17.3**	**-**				
	CL1	-20.5	0.2	0.3		5.3	0.3	10	0	-18.1	-2.4	-2.3	-3.2	-18.2	-17.2
	CL2	-18.5	0.2	0.3		2.6	0.2	9	0	-17.9	-0.6				
	Roy L5	-0.4	0.2	0.6		4.3	0.4	14	2	-1.4	0.9	1.5	0.5	-1.9	-0.9
	Roy L6	-0.7	0.2	1.0		11.1	0.7	16	0	-1.2	0.5	0.8	1.0	-1.5	-1.7
	BAH	-1.7	0.4	0.3		3.9	0.3	5	0	-2.6	0.9	3.3	2.4	-4.9	-4.0
	BAH	-1.8	0.4	0.2		3.6	0.3	4	0	-2.6	0.9	3.3	2.4	-5.0	-4.1

R9	**HM-27_HM-22**														
	CL4 - normalizing RM	**-17.3**	**0.1**	**0.3**	**0.1**	**4.8**	**0.2**	**43**	**1**	**-17.3**	**-**				
	Roy L5	0.1	0.4	0.4		7.5	0.4	6	0	-1.4	1.5	1.5	0.5	-1.3	-0.4
	Roy L6	-0.2	0.2	0.1		0.2	0.1	6	1	-1.2	1.0	0.8	1.0	-1.0	-1.2
R9	**HM-23B**														
	CL4 - normalizing RM	**-17.3**	**0.1**	**0.3**	**0.1**	**6.2**	**0.2**	**53**	**0**	**-17.3**	**-**				
R9	**HM-27_AZL**														
	CL4 - normalizing RM	**-17.3**	**0.1**	**0.3**	**0.1**	**2.2**	**0.2**	**46**	**0**	**-17.3**	**-**				
R9	**HM-16C**														
	CL4 - normalizing RM	**-17.3**	**0.2**	**0.4**	**0.2**	**7.1**	**0.3**	**14**	**0**	**-17.3**	**-**				
R10	**HM-17**														
	CL4 - normalizing RM	**-17.3**	**0.1**	**0.3**	**0.1**	**2.1**	**0.2**	**79**	**0**	**-17.3**	**-**				
R10	**HM-27_HM-18**														
	CL4 - normalizing RM	**-17.3**	**0.1**	**0.2**	**0.1**	**3.9**	**0.2**	**45**	**0**	**-17.3**	**-**				
	Roy L5	-1.8	0.2	0.3		4.8	0.3	10	0	-1.4	-0.4	0.5	0.3	-2.3	-2.1
	Roy L6	-1.7	0.1	0.2		2.9	0.2	10	0	-1.2	-0.5	0.2	0.4	-1.9	-2.1
	Stop1-6-D1	0.0	0.1	0.2		2.2	0.2	10	0	-0.7	0.7	1.3	0.8	-1.2	-0.7
R10	**HM-27_HM-23**														

CL4 - normalizing RM	**-17.3**	**0.1**	**0.4**	**0.1**	**11.3**	**0.3**	**92**	**0**	**-17.3**	**-**				
Win 03A	0.0	0.1	0.2		1.7	0.1	15	0	-2.1	2.1	1.5	1.9	-1.4	-1.9
Win 03A	-0.4	0.2	0.2		3.7	0.2	10	1	-2.1	1.7	1.5	1.9	-1.8	-2.2
Roy L5	0.1	0.1	0.2		2.3	0.2	13	1	-1.4	1.5	0.5	0.3	-0.4	-0.2
Roy L5	-0.8	0.2	0.3		4.0	0.2	10	0	-1.4	0.6	0.5	0.3	-1.3	-1.1
Roy L6	0.7	0.1	0.3		8.3	0.2	18	1	-1.2	1.9	0.2	0.4	0.5	0.3
Roy L6	-1.7	0.2	0.3		8.0	0.3	10	2	-1.2	-0.5	0.2	0.4	-1.9	-2.1

(*) Measured Bias

Declaration of interests

☒ The authors declare that they have no known competing financial interests or personal relationships that could have appeared to influence the work reported in this paper.

☐The authors declare the following financial interests/personal relationships which may be considered as potential competing interests:

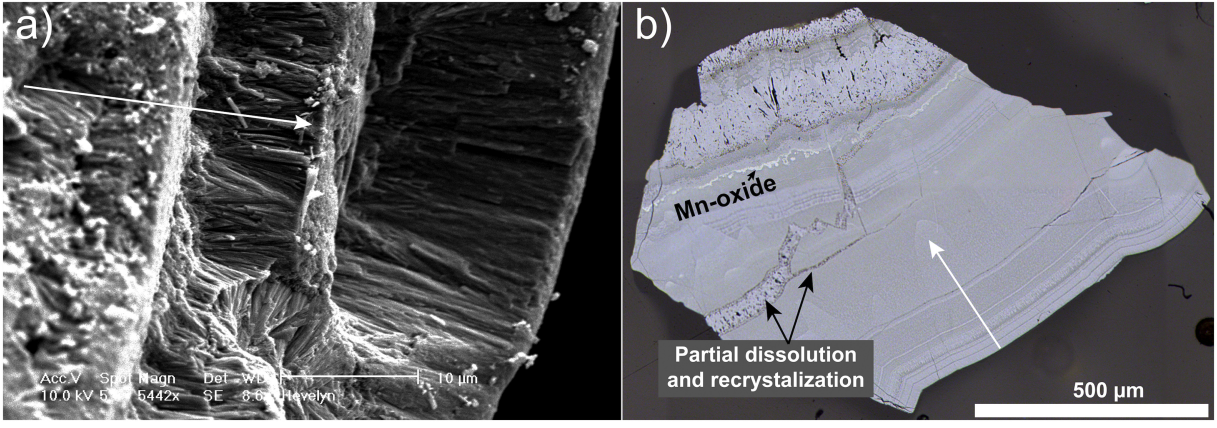
a)
Acc.V Spot Magn Det WD
10.0 kV 5 5442x SE 8.6
Hevelyn
10 µm
b)
Mn-oxide
Partial dissolution
and recrystalization
500 µm

Figure 1

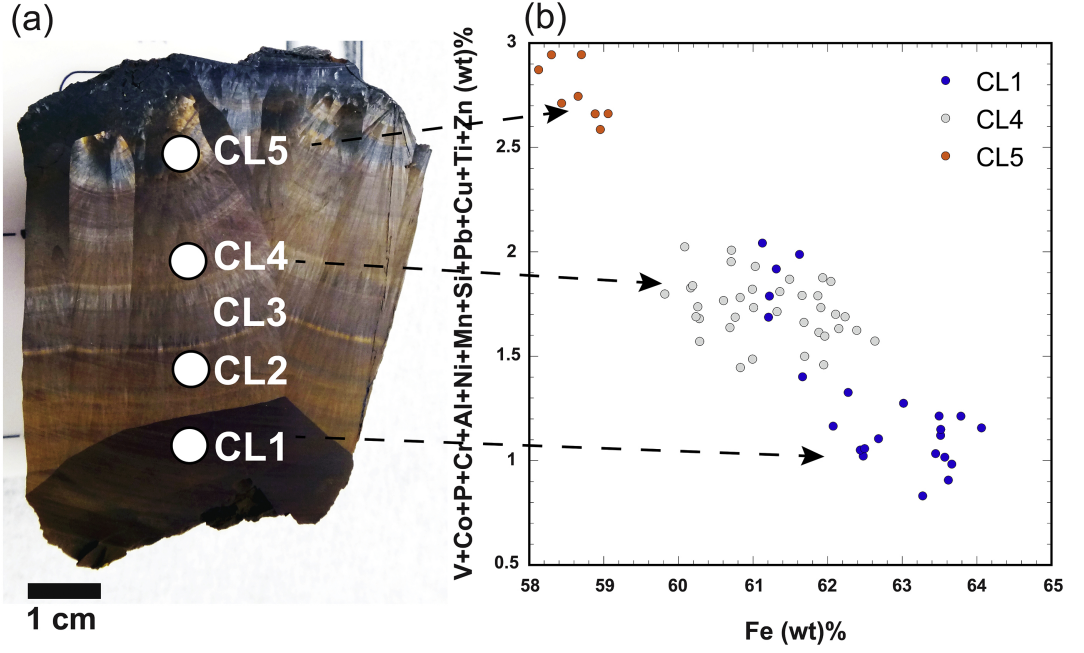
(a)
CL5
CL4
CL3
CL2
CL1
1 cm
(b)
CL1
CL4
CL5
V+Co+P+Cr+Al+Ni+Mn+Si+Pb+Cu+Ti+Zn (wt)%
Fe (wt)%
3
2.5
2
1.5
1
0.5
58
59
60
61
62
63
64
65

Figure 2

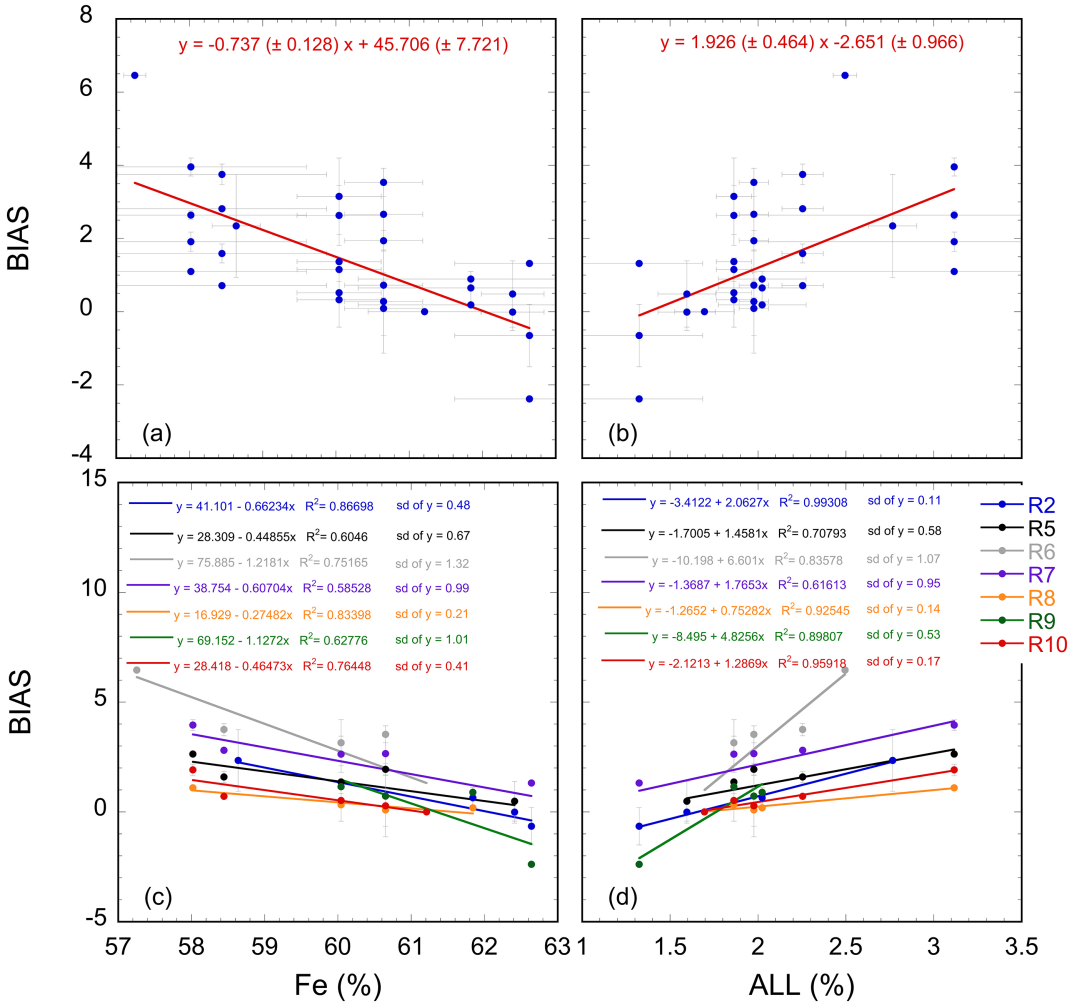
y = -0.737 (± 0.128) x + 45.706 (± 7.721)
y = 1.926 (± 0.464) x -2.651 (± 0.966)
BIAS
(a)
(b)
y = 41.101 - 0.66234x R2= 0.86698 sd of y = 0.48
y = 28.309 - 0.44855x R2= 0.6046 sd of y = 0.67
y = 75.885 - 1.2181x R2= 0.75165 sd of y = 1.32
y = 38.754 - 0.60704x R2= 0.58528 sd of y = 0.99
y = 16.929 - 0.27482x R2= 0.83398 sd of y = 0.21
y = 69.152 - 1.1272x R2= 0.62776 sd of y = 1.01
y = 28.418 - 0.46473x R2= 0.76448 sd of y = 0.41
y = -3.4122 + 2.0627x R2= 0.99308 sd of y = 0.11
y = -1.7005 + 1.4581x R2= 0.70793 sd of y = 0.58
y = -10.198 + 6.601x R2= 0.83578 sd of y = 1.07
y = -1.3687 + 1.7653x R2= 0.61613 sd of y = 0.95
y = -1.2652 + 0.75282x R2= 0.92545 sd of y = 0.14
y = -8.495 + 4.8256x R2= 0.89807 sd of y = 0.53
y = -2.1213 + 1.2869x R2= 0.95918 sd of y = 0.17
R2
R5
R6
R7
R8
R9
R10
BIAS
(c)
(d)
Fe (%)
ALL (%)

Figure 3

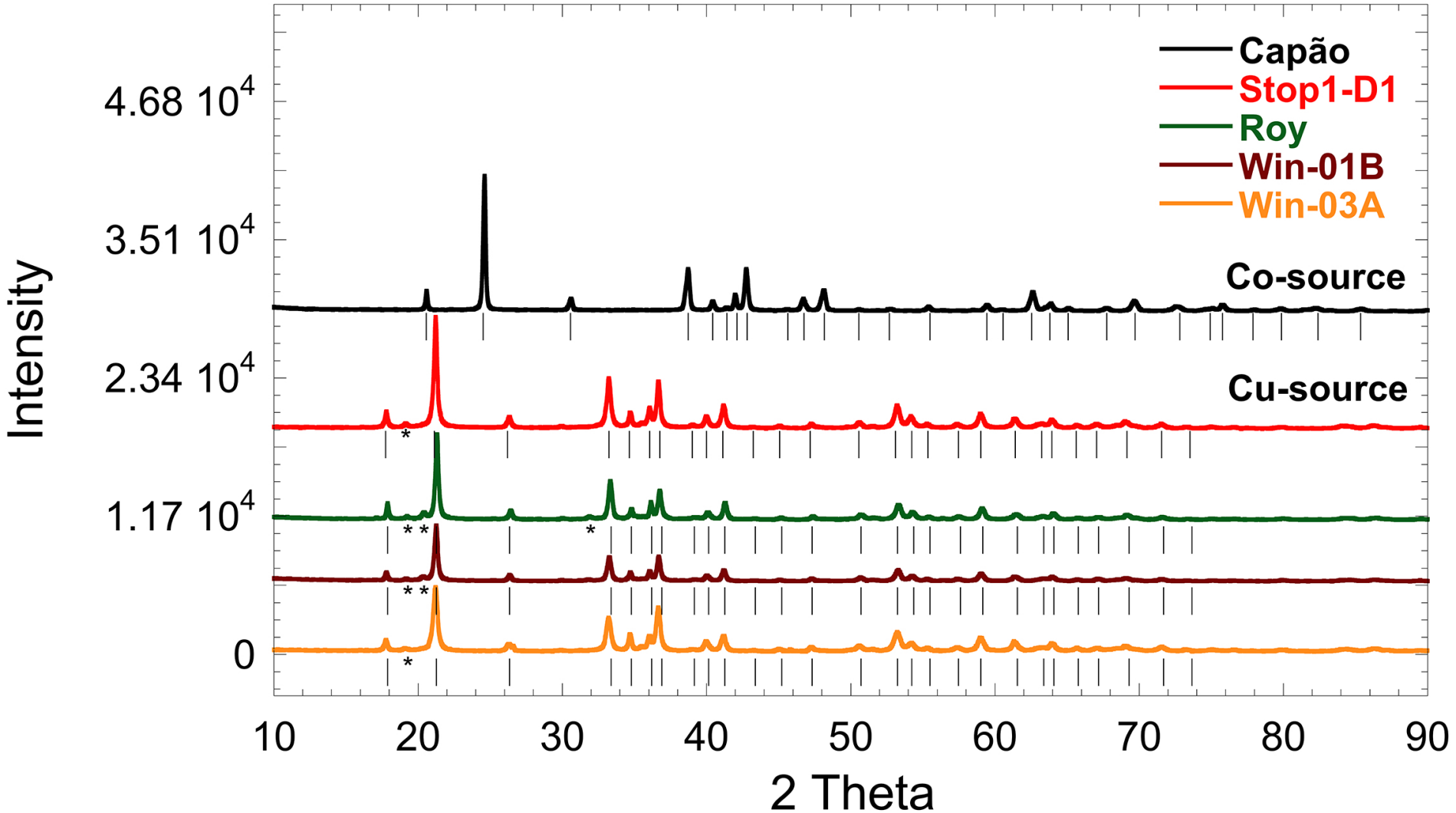
Capão
Stop1-D1
Roy
Win-01B
Win-03A
Co-source
Cu-source
Intensity
4.68 10^4
3.51 10^4
2.34 10^4
1.17 10^4
0
10
20
30
40
50
60
70
80
90
2 Theta

Figure 4

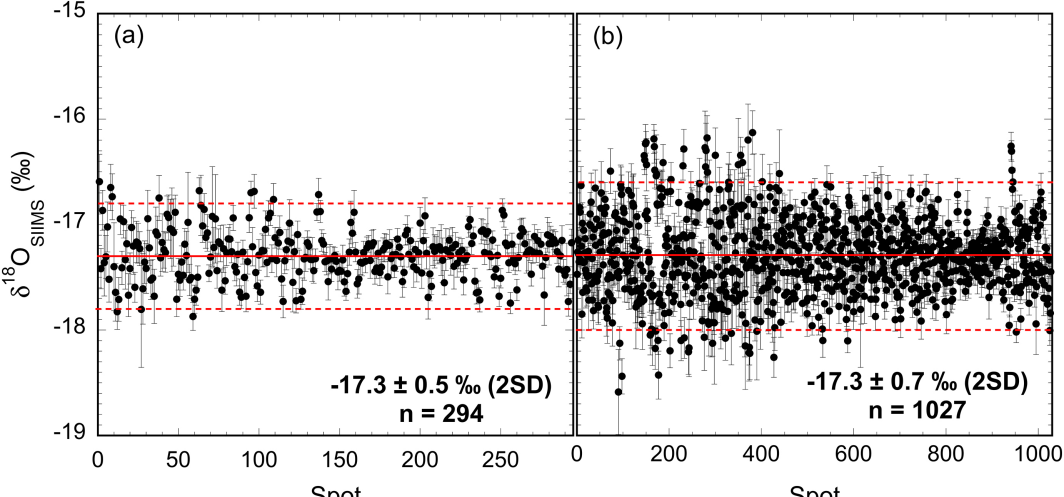
(a)
(b)
-15
-16
-17
-18
-19
δ18OSIIMS (‰)
-17.3 ± 0.5 ‰ (2SD)
n = 294
-17.3 ± 0.7 ‰ (2SD)
n = 1027
0
50
100
150
200
250
0
200
400
600
800
1000
Spot
Spot

Figure 5

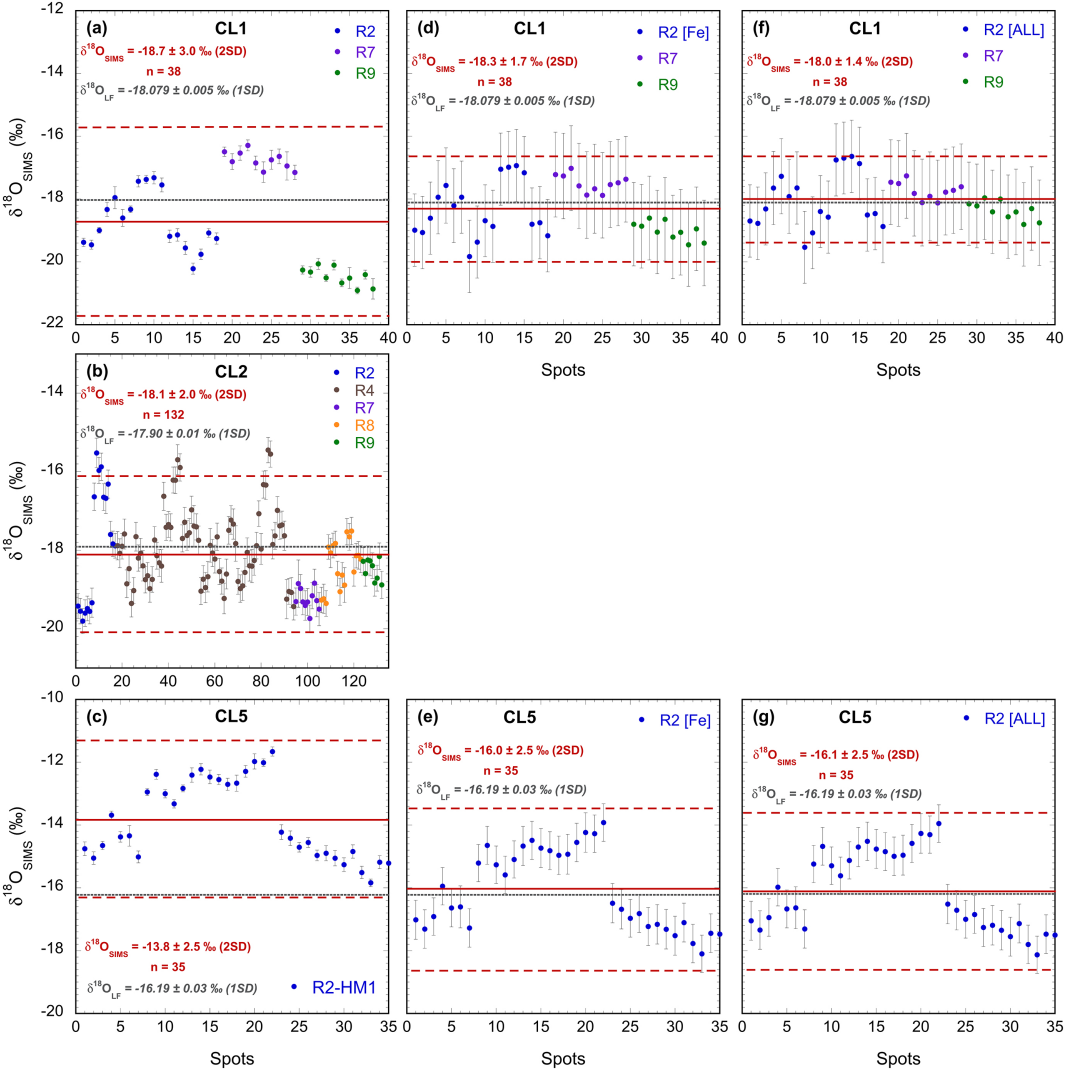
(a)
CL1
R2
R7
R9
δ18OSIMS = -18.7 ± 3.0 ‰ (2SD)
n = 38
δ18OLF = -18.079 ± 0.005 ‰ (1SD)
(d)
CL1
R2 [Fe]
R7
R9
δ18OSIMS = -18.3 ± 1.7 ‰ (2SD)
n = 38
δ18OLF = -18.079 ± 0.005 ‰ (1SD)
(f)
CL1
R2 [ALL]
R7
R9
δ18OSIMS = -18.0 ± 1.4 ‰ (2SD)
n = 38
δ18OLF = -18.079 ± 0.005 ‰ (1SD)
(b)
CL2
R2
R4
R7
R8
R9
δ18OSIMS = -18.1 ± 2.0 ‰ (2SD)
n = 132
δ18OLF = -17.90 ± 0.01 ‰ (1SD)
(c)
CL5
δ18OSIMS = -13.8 ± 2.5 ‰ (2SD)
n = 35
δ18OLF = -16.19 ± 0.03 ‰ (1SD)
R2-HM1
(e)
CL5
R2 [Fe]
δ18OSIMS = -16.0 ± 2.5 ‰ (2SD)
n = 35
δ18OLF = -16.19 ± 0.03 ‰ (1SD)
(g)
CL5
R2 [ALL]
δ18OSIMS = -16.1 ± 2.5 ‰ (2SD)
n = 35
δ18OLF = -16.19 ± 0.03 ‰ (1SD)
δ18OSIMS (‰)
Spots

Figure 6

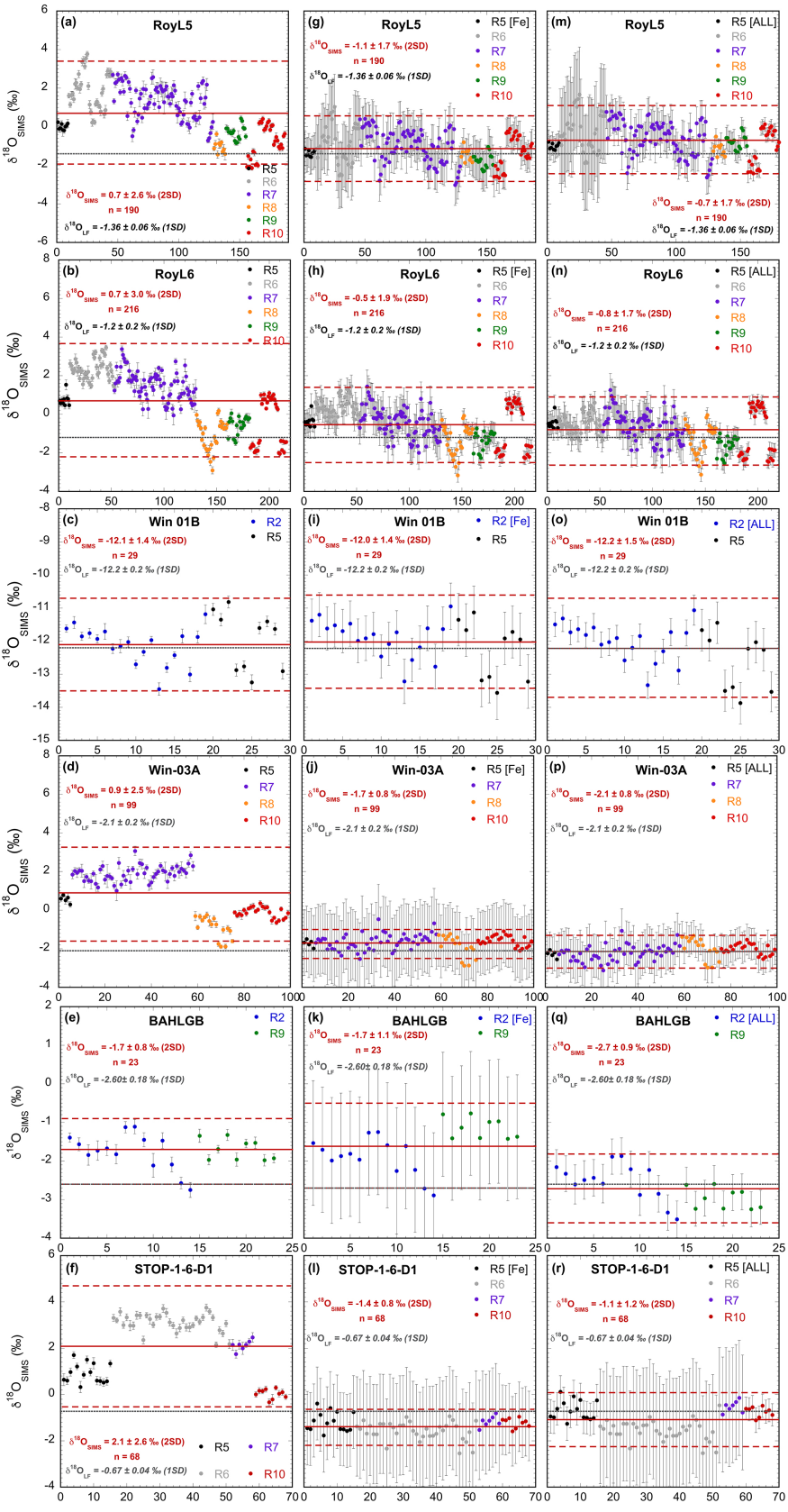
(a)
RoyL5
δ18OSIMS = 0.7 ± 2.6 ‰ (2SD)
n = 190
δ18OLF = -1.36 ± 0.06 ‰ (1SD)
R5
R6
R7
R8
R9
R10
(g)
RoyL5
δ18OSIMS = -1.1 ± 1.7 ‰ (2SD)
n = 190
δ18OLF = -1.36 ± 0.06 ‰ (1SD)
R5 [Fe]
R6
R7
R8
R9
R10
(m)
RoyL5
δ18OSIMS = -0.7 ± 1.7 ‰ (2SD)
n = 190
δ18OLF = -1.36 ± 0.06 ‰ (1SD)
R5 [ALL]
R6
R7
R8
R9
R10
(b)
RoyL6
δ18OSIMS = 0.7 ± 3.0 ‰ (2SD)
n = 216
δ18OLF = -1.2 ± 0.2 ‰ (1SD)
R5
R6
R7
R8
R9
R10
(h)
RoyL6
δ18OSIMS = -0.5 ± 1.9 ‰ (2SD)
n = 216
δ18OLF = -1.2 ± 0.2 ‰ (1SD)
R5 [Fe]
R6
R7
R8
R9
R10
(n)
RoyL6
δ18OSIMS = -0.8 ± 1.7 ‰ (2SD)
n = 216
δ18OLF = -1.2 ± 0.2 ‰ (1SD)
R5 [ALL]
R6
R7
R8
R9
R10
(c)
Win 01B
δ18OSIMS = -12.1 ± 1.4 ‰ (2SD)
n = 29
δ18OLF = -12.2 ± 0.2 ‰ (1SD)
R2
R5
(i)
Win 01B
δ18OSIMS = -12.0 ± 1.4 ‰ (2SD)
n = 29
δ18OLF = -12.2 ± 0.2 ‰ (1SD)
R2 [Fe]
R5
(o)
Win 01B
δ18OSIMS = -12.2 ± 1.5 ‰ (2SD)
n = 29
δ18OLF = -12.2 ± 0.2 ‰ (1SD)
R2 [ALL]
R5
(d)
Win-03A
δ18OSIMS = 0.9 ± 2.5 ‰ (2SD)
n = 99
δ18OLF = -2.1 ± 0.2 ‰ (1SD)
R5
R7
R8
R10
(j)
Win-03A
δ18OSIMS = -1.7 ± 0.8 ‰ (2SD)
n = 99
δ18OLF = -2.1 ± 0.2 ‰ (1SD)
R5 [Fe]
R7
R8
R10
(p)
Win-03A
δ18OSIMS = -2.1 ± 0.8 ‰ (2SD)
n = 99
δ18OLF = -2.1 ± 0.2 ‰ (1SD)
R5 [ALL]
R7
R8
R10
(e)
BAHLGB
δ18OSIMS = -1.7 ± 0.8 ‰ (2SD)
n = 23
δ18OLF = -2.60± 0.18 ‰ (1SD)
R2
R9
(k)
BAHLGB
δ18OSIMS = -1.7 ± 1.1 ‰ (2SD)
n = 23
δ18OLF = -2.60± 0.18 ‰ (1SD)
R2 [Fe]
R9
(q)
BAHLGB
δ18OSIMS = -2.7 ± 0.9 ‰ (2SD)
n = 23
δ18OLF = -2.60± 0.18 ‰ (1SD)
R2 [ALL]
R9
(f)
STOP-1-6-D1
δ18OSIMS = 2.1 ± 2.6 ‰ (2SD)
n = 68
δ18OLF = -0.67 ± 0.04 ‰ (1SD)
R5
R6
R7
R10
(l)
STOP-1-6-D1
δ18OSIMS = -1.4 ± 0.8 ‰ (2SD)
n = 68
δ18OLF = -0.67 ± 0.04 ‰ (1SD)
R5 [Fe]
R6
R7
R10
(r)
STOP-1-6-D1
δ18OSIMS = -1.1 ± 1.2 ‰ (2SD)
n = 68
δ18OLF = -0.67 ± 0.04 ‰ (1SD)
R5 [ALL]
R6
R7
R10
δ18OSIMS (‰)
Spots

Figure 7

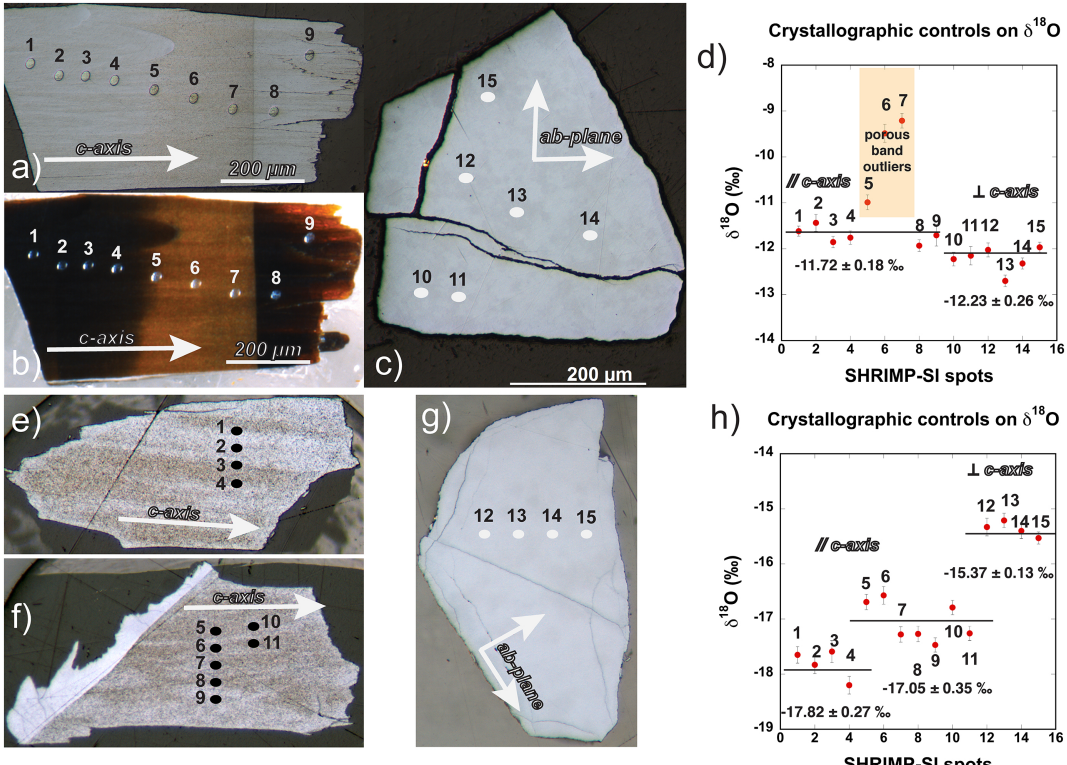
a)
1 2 3 4 5 6 7 8 9
c-axis
200 µm
b)
1 2 3 4 5 6 7 8 9
c-axis
200 µm
c)
15
ab-plane
12
13
14
10 11
200 µm
d)
Crystallographic controls on δ18O
porous band outliers
6 7
// c-axis
⊥ c-axis
-11.72 ± 0.18 ‰
-12.23 ± 0.26 ‰
δ18O (‰)
SHRIMP-SI spots
e)
1 2 3 4
c-axis
f)
c-axis
5 6 7 8 9
10 11
g)
12 13 14 15
ab-plane
h)
Crystallographic controls on δ18O
// c-axis
⊥ c-axis
-15.37 ± 0.13 ‰
-17.05 ± 0.35 ‰
-17.82 ± 0.27 ‰
δ18O (‰)
SHRIMP-SI spots

Figure 8

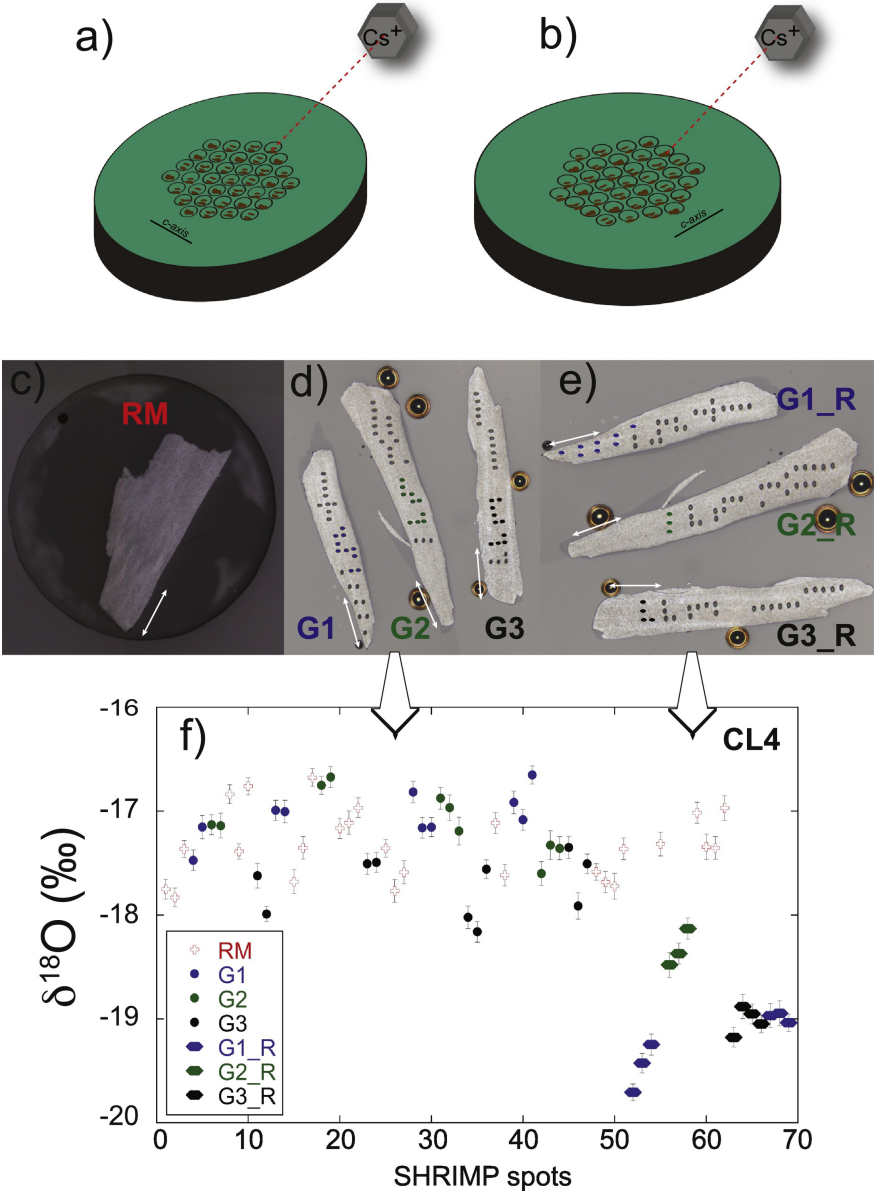
a)
Cs+
c-axis
b)
Cs+
c-axis
c)
RM
d)
G1
G2
G3
e)
G1_R
G2_R
G3_R
f)
CL4
δ18O (‰)
-16
-17
-18
-19
-20
0
10
20
30
40
50
60
70
SHRIMP spots
RM
G1
G2
G3
G1_R
G2_R
G3_R

Figure 9

Precipitation Temperature: 22°C

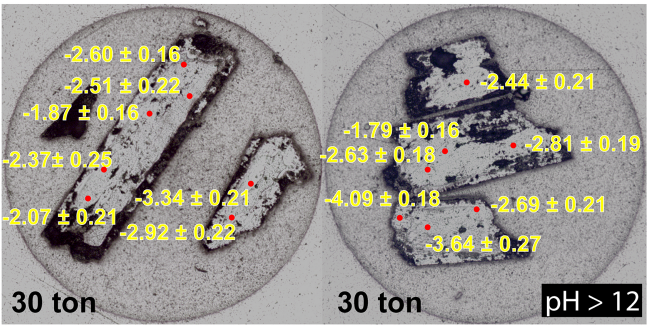

Precipitation Temperature: 30°C

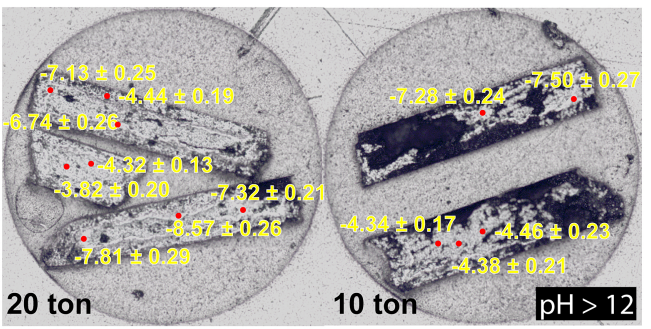

Precipitation Temperature: 40°C

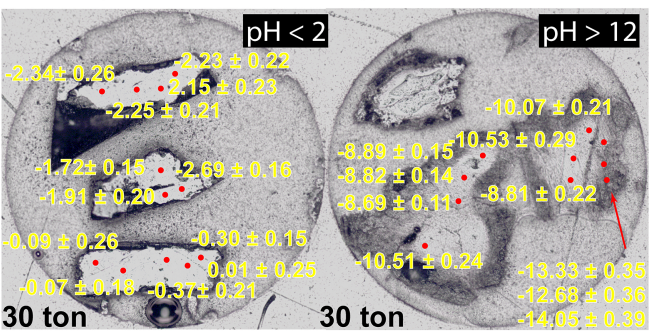

Figure 10

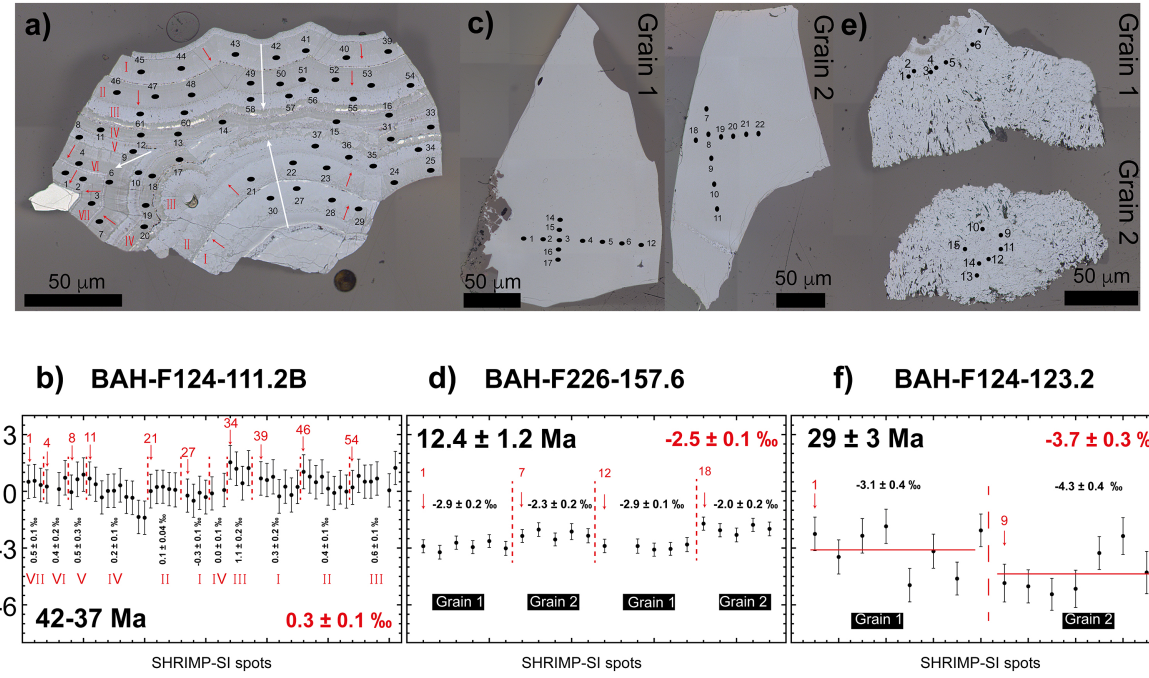
a)
50 µm
c)
Grain 1
Grain 2
50 µm
e)
Grain 1
Grain 2
50 µm
b) BAH-F124-111.2B
δ18O (‰)
42-37 Ma
0.3 ± 0.1 ‰
SHRIMP-SI spots
d) BAH-F226-157.6
12.4 ± 1.2 Ma
-2.5 ± 0.1 ‰
-2.9 ± 0.2 ‰
-2.3 ± 0.2 ‰
-2.9 ± 0.1 ‰
-2.0 ± 0.2 ‰
Grain 1
Grain 2
Grain 1
Grain 2
SHRIMP-SI spots
f) BAH-F124-123.2
29 ± 3 Ma
-3.7 ± 0.3 ‰
-3.1 ± 0.4 ‰
-4.3 ± 0.4 ‰
Grain 1
Grain 2
SHRIMP-SI spots

Figure 11

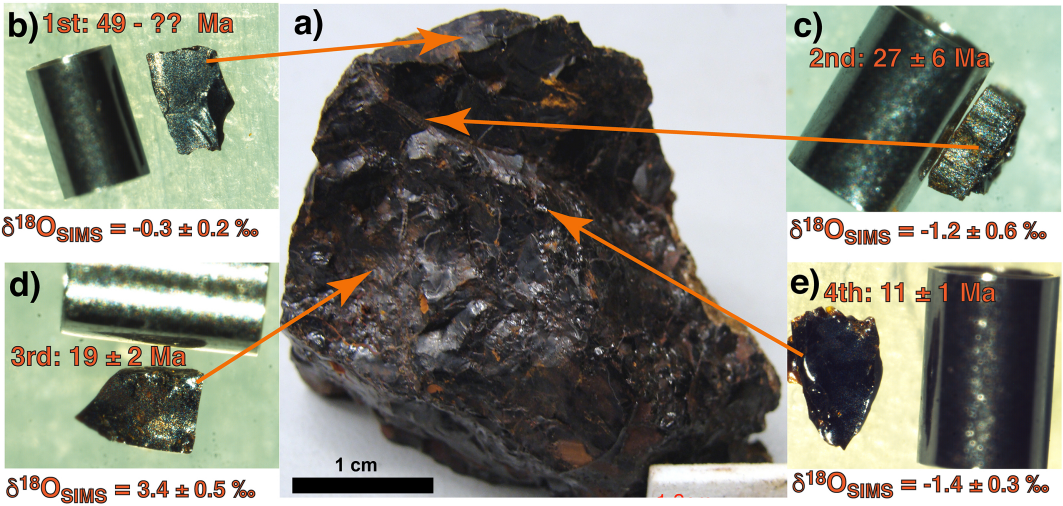
b) 1st: 49 - ?? Ma
a)
c)
2nd: 27 ± 6 Ma
δ18OSIMS = -0.3 ± 0.2 ‰
δ18OSIMS = -1.2 ± 0.6 ‰
d)
3rd: 19 ± 2 Ma
e) 4th: 11 ± 1 Ma
1 cm
δ18OSIMS = 3.4 ± 0.5 ‰
δ18OSIMS = -1.4 ± 0.3 ‰

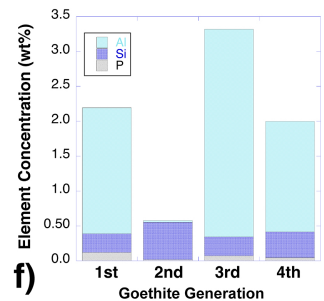
Element Concentration (wt%)
3.5
3.0
2.5
2.0
1.5
1.0
0.50
0.0
Al
Si
P
1st
2nd
3rd
4th
Goethite Generation
f)

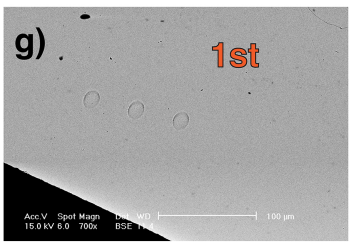
g)
1st

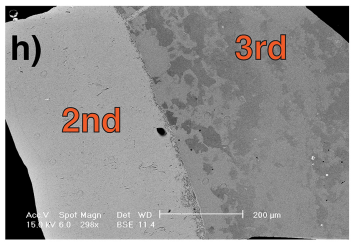
h)
3rd
2nd

Figure 12